جامعة الجوف
Jouf University

# Aljouf University Science and Engineering Journal

## (AUSEJ)

### Peer-Reviewed International Journal

# Jouf University Science and Engineering Journal

*Peer-reviewed International Journal*

*Designed and Edited by Prof. Abdelazim M. Mebed*

من سورة يوسف - الآية: 76

*Dear professional colleagues, researchers and fellow students:*

We are pleased to present the second issue of Volume VIII of the Journal of Science and Engineering (JUSEJ). JUSEJ was established under the generous sponsorship of the former rector of Jouf University, Prof. Ismail Muhammad Al-Bishri, since 2014, and the continuous support of the current president of the University, Prof. Muhammad Al-Shaya. Its maturity is an outcome of the consistent support of high-performing authors, a supportive and professional dedicated reviewers, many vigorous and conscientious editorial boards and collective input from the editorial board members. Various researchers who are active in the above field have been enrolled for providing the necessary impetus for the new journal. We are quite hopeful and shall be grateful to the service that these eminent scientists shall provide to the growth of JUSEJ. We are certain that the renowned scientists and academicians both from the industry and academic institutions all over the world will be enriched by sharing their research experiences through JUSEJ. We are happy to invite you to submit your valuable research works in URP journals. We strongly believe that our journal will help to develop your own professional career.

*Thanks*
*Editors*

## Editorial Board

## Focus and Scope

With its vision to promote science and scientific knowledge to everybody, Jouf Science and Engineering Journal (JUSEJ) is an international peer-reviewed journal owned by Jouf University with a focused aim of promoting and publishing original high quality research papers dealing with basic and engineering science. JUSEJ publishes rigorous and original contributions in the Science disciplines of

| | | |
|---|---|---|
| Physics | Engineering, All Fields | Applied Biology |
| Chemistry | Mathematics & Statistics | Physiology |
| Biochemistry | Computer Science | Plant Biology |
| Biological Sciences | Genomics | Population Biology |
| Biophysics | Geology | Food & Food Technology |
| Petroleum & Gas | Environment | Robotics |
| Cell Biology | Solid State Technology | Signal Transduction |
| Parasitological Science | Communication & IT | Space Science |
| Developmental Biology | Microbiology | Energy |
| Genetics | Zoology | Textile Industry & Fabrics |
| Construction | Nanotechnology | Toxicology |

III

The papers published in Jouf Science and Engineering Journal (JUSEJ) should present novel results and have either theoretical significance or practical utility or both. They may be presented in the form of full articles, short communications or state-of-the-art reviews.

All contributions will be rigorously reviewed to ensure both scientific quality and technical relevance. Revisions of manuscripts may thus be required.

Manuscripts must be submitted in the English language and authors must ensure that the article has not been published or submitted for publication elsewhere in any format, and that there are no ethical concerns with the contents or data collection. The authors warrant that the information submitted is not redundant and respects general guidelines of ethics in publishing. All papers are evaluated by at least two international referees, who are known scholars in their fields.

## Objectives

The main objective of JUSEJ is to provide an international forum for academics, researchers, industry leaders, and policy makers to investigate and exchange novel ideas and disseminate knowledge and information covering the broad range of natural science and industrial activities. In addition, it aims to establish an effective channel of communication between policy makers, government agencies, academic and research institutions and persons concerned with basic science and its applications. It also aims to promote and coordinate developments in the fields of natural science, engineering science and other related fields. The international dimension is emphasized in order to overcome cultural and national barriers and to meet the needs of accelerating ecological and technological advances in all industries and the global society and economy.

## Open Access Policy

This journal provides immediate open access to its content on the principle that making research freely available to the public supports a greater global exchange of knowledge.

All published manuscripts will be available on the Journals website **http://vrgs.ju.edu.sa/#**. We strongly believe that our journal will help to develop your own professional career. You can communicate with us at any time, throughout the publishing process.

## EDITORIAL OFFICE & COMMUNICATION

# TABLE OF CONTENTS

# GUIDE FOR AUTHOR

## TYPES OF CONTRIBUTIONS

Original research papers and occasional reviews, short communications, letters, letters to the editor and news items. Please ensure that you indicate clearly the appropriate article type when making your submission.

## BEFORE YOU BEGIN

### *Ethical guidelines*
### Confidentiality
All material submitted to Science Journal of Jouf University (SJJU), accordingly to Jouf Science, Engineering Journal (JUSEJ) remains confidential, and the Editor operates a peer review system in which the identity of the referees is protected.

### Duplicate publication
Duplicate publication is the publication of the same paper or substantially similar papers in more than one journal. Authors must explain in the submission letter any prior publication of the same or a substantially similar paper, and should explain any circumstances that might lead the Editor or reviewers to believe that the paper may have been published elsewhere (for example, when the title of a submitted paper is the same as or similar to the title of a previously published article).

If work that makes up more than 10% of the manuscript submitted to JUSEJ has been published elsewhere, please provide a copy of the published article in order that the Editor can make a judgment on the amount of overlap without delay. If a member of the editorial board learns that work under consideration has previously been published in whole or in part,

the Editor may return the paper without review, reject the paper, announce the duplication publicly in an editorial and/or contact the authors' employers.

### Submission of manuscripts to more than one journal
Authors may not send the same manuscript to more than one journal concurrently. If this occurs, the Editor may return the paper without review, reject the paper, contact the Editor of the other journal(s) in question and/or contact the authors' employers.

### Plagiarism and scientific misconduct
Plagiarism is the use of others' published and unpublished ideas or words (or other intellectual property) without due reference or permission and/or their presentation as new and original points. Plagiarism is serious scientific misconduct and will be dealt with accordingly. All papers submitted to the journal is cheched with *iThenticate* program for plagiarism. We define plagiarism as a case in which a paper reproduces another work with at least 15% similarity and without citation.

If evidence of plagiarism is found before or after acceptance or after publication of the paper, the author will be offered a chance to defend his/her paper. If the arguments are found to be unsatisfactory, the manuscript will be retracted and authors found to have been guilty of plagiarism will no longer have papers accepted for publication by JUSEJ.



iThenticate compares submitted documents to extensive data repositories to create a

comprehensive Similarity Report, which highlights and provides links to any significant text matches, helping to ensure that you are submitting an original and well-attributed document.

### Data auditing

The journal reserves the right to view original figures and data and may make periodic requests to see these.

### Conflict of interest

All authors are requested to disclose any actual or potential conflict of interest including any financial, personal or other relationships with other people or organizations within three years of beginning the submitted work that could inappropriately influence, or be perceived to influence, their work.

### Submission declaration

Submission of an article implies that the work described has not been published previously (except in the form of an abstract or as part of a published lecture or academic thesis or as an electronic preprint, that it is not under consideration for publication elsewhere, that its publication is approved by all authors and tacitly or explicitly by the responsible authorities where the work was carried out, and that, if accepted, it will not be published elsewhere including electronically in the same form, in English or in any other language, without the written consent of the copyright-holder.

### Changes in authorship

Requests to add or remove an author, or to rearrange the author names, must be sent to the Journal Manager from the corresponding author of the accepted manuscript *before the accepted manuscript is published* and must include: (a) the reason for the addition, removal, or rearrangement of the authors᾿ names and (b) written confirmation (e-mail, fax, letter) from all authors that they agree with the addition,

removal or rearrangement. In the case of addition or removal of authors, this includes confirmation from the author being added or removed. Requests that are not sent by the corresponding author will be forwarded by the Journal Manager to the corresponding author, who must follow the procedure as described above. Note that: (1) Journal Managers will inform the Journal Editors of any such requests and (2) publication of the accepted manuscript is suspended until authorship has been agreed.

### Copyright

Upon acceptance of an article, authors will be asked to complete a 'Journal Publishing Agreement' An e-mail will be sent to the corresponding author confirming receipt of the manuscript together with a 'Journal Publishing Agreement'.

Subscribers may reproduce tables of contents or prepare lists of articles, including abstracts for internal circulation within their institutions. Permission of the Publisher is required for resale or distribution outside the institution and for all other derivative works, including compilations and translations.

If excerpts from other copyrighted works are included, the author(s) must obtain written permission from the copyright owners and credit the source(s) in the article.

### Retained author rights

As an author you (or your employer or institution) have the right to use your articles for a wide range of scholarly purposes.

### Role of the funding source

You are requested to identify who provided financial support for the conduct of the research and/or preparation of the article and to briefly describe the role of the sponsor(s), if any, in study design; in the collection, analysis and interpretation of data; in the writing of the report; and in the decision to submit the article

for publication. If the funding source(s) had no such involvement then this should be stated

## Subscription
Articles are made available to subscribers as well as developing countries and patient groups

### *Language (usage and editing services)*
Please write your text in good English (American or British usage is accepted, but not a mixture of these). If the English language is used, extra abstract in Arabic should be provided.

### *Submission*
To submit your paper, please send your manuscripts by e-mail to the Editor (AJBSE@ju.edu.sa). You must submit the manuscript in a single electronic file. The manuscript should be edited using Microsoft (MS) Word (2003 up to 2010, with .doc or .docx extension)

### *Referees*
Please submit, with the manuscript, the names, addresses and e-mail addresses of three potential referees. Note that the Editor retains the only one who has the right to decide whether or not the suggested reviewers are used.

## PREPARATION

### *Use of word processing software*
Manuscripts must be in an electronic format that meets the following specifications:

- Do not submit a manuscript file as a PDF file. Remove line numbering.
- The manuscript file—with tables and figures placed at the end of the file, each on a separate page—should be in Microsoft Word (2003 up to 2010, with .doc or .docx extension).
- Do not use the Microsoft Word "Styles and Formatting" or "Track Changes" features in the file.

- Tables should be in MS Word (.doc or .docx), one table to a page using hard page breaks.
- Figures (graphics of any kind) should be placed at the end of the Word document as images, one figure to a page using hard page breaks.
- Equations may be created and inserted as part of the text, or they may be submitted as images embedded within the text.

## ARTICLE STRUCTURE

### Manuscript Page setup
- Margins: 25.4 mm (1 in.) top, 25.4 mm (1 in.) left; adjust the settings for bottom and right margins so that the text area is not more than 165.1 mm by 228.6 mm (6.5 in. by 9 in.)
- Font (typeface): Times New Roman, no smaller than 10 points.
- Numbering: Insert page numbers at upper right of each page; insert name(s) of author(s) at upper left of each page
- Text: Single-spaced.
- Paragraphs: Indent first line 12.7 mm (0.5 in.); do not use an extra line space between paragraphs; do not indent first line after a subhead.

Subheads: All subheads should be flush with the left margin, with one line space above. Subsections should be numbered 1.1 (then 1.1.1, 1.1.2, ...), 1.2, etc. (the abstract is not included in section numbering).

### FIRST-LEVEL SUBHEAD
(all capitals, boldface, on separate line)
### Second-Level Subhead
(initial capitals, boldface, on separate line)
### *Third-Level Subhead*
(initial capitals, italic, on separate line)

**Fourth-Level Subhead** (initial capitals, boldface, on same line as text, with extra letter space between the subhead and text)

*Fifth-Level Subhead* (initial capitals, italic, on same line as text, with extra letter space between the subhead and text)

• Bulleted and numbered lists: Indent first line 12.7 mm (0.5 in.); do not indent for text runovers.

**Table Titles and Figure Captions:**

**TABLE 5 Effects of All Factors**
(Insert title above the table; "Table" is all capitals; title is initial capitals; all types are boldfaced;
Extra space, but no punctuation after number; no punctuation at end of title.)

**FIGURE 3 Example of results**.
(Insert caption below the figure; "Figure" is all capitals; caption is sentence case; all type is boldface; extra space but no punctuation after number; period at end of caption.)

**Body of the manuscript**

*Introduction*
State the objectives of the work and provide an adequate background, avoiding a detailed literature survey or a summary of the results.

*Materials and methods*
Provide sufficient detail to allow the work to be reproduced. Methods already published should be indicated by a reference: only relevant modifications should be described.

*Theory/calculation*
A Theory section should extend, not repeat, the background to the article already dealt with in the Introduction and lay the foundation for further work. In contrast, a Calculation section

represents a practical development from a theoretical basis.

*Results*
Results should be clear and concise.

*Discussion*
This should explore the significance of the results of the work, not repeat them. A combined Results and Discussion section is often appropriate. Avoid extensive citations and discussion of published literature.

*Conclusions*
The main conclusions of the study may be presented in a short Conclusions section, which may stand alone or form a subsection of a Discussion or Results and Discussion section.

*Appendices*
If there is more than one appendix, they should be identified as A, B, etc. Formulae and equations in appendices should be given separate numbering: Eq. (A.1), Eq. (A.2), etc.; in a subsequent appendix, Eq. (B.1) and so on. Similarly for tables and figures: Table A.1; Fig. A.1, etc.

***Essential title page information***
• ***Title.*** Concise and informative. Titles are often used in information-retrieval systems. Avoid
abbreviations and formulae where possible. The title should be all capitals.
• ***Author names and affiliations.*** Where the family name may be ambiguous (e.g., a double name), please indicate this clearly. Present the authors' affiliation addresses (where the actual work was done) below the names. Indicate all affiliations with a lower-case superscript letter immediately after the author's name and in front of the appropriate address. Provide the full postal address of each affiliation, including the

country name, and, if available, the e-mail address of each author.

• *Corresponding author.* Clearly indicate who will handle correspondence at all stages of refereeing and publication, also post-publication. **Ensure that phone numbers (with country and area code) are provided in addition to the e-mail address and the complete postal address. Contact details must be kept up to date by the corresponding author.**

• *Present/permanent address.* If an author has moved since the work described in the article was done, or was visiting at the time, a 'Present address' (or 'Permanent address') may be indicated as a footnote to that author's name. The address at which the author actually did the work must be retained as the main, affiliation address. Superscript Arabic numerals are used for such footnotes.

### Abstract

A concise and factual abstract is required. The abstract should state briefly the purpose of the research, the principal results and major conclusions. An abstract is often presented separately from the article, so it must be able to stand alone. For this reason, References should be avoided, but if essential, then cite the author(s) and year(s). Also, non-standard or uncommon abbreviations should be avoided, but if essential they must be defined at their first mention in the abstract itself.

### Keywords

Immediately after the abstract, provide a maximum of 6 keywords, using American spelling and
avoiding general and plural terms and multiple concepts (avoid, for example, 'and', 'of'). Be sparing with abbreviations: only abbreviations firmly established in the field may be eligible. These keywords will be used for indexing purposes.

### Abbreviations

Define abbreviations that are not standard in this field in a footnote to be placed on the first page of the article. Such abbreviations that are unavoidable in the abstract must be defined at their first mention there, as well as in the footnote. Ensure consistency of abbreviations throughout the article.

### Acknowledgements

Collate acknowledgements in a separate section at the end of the article before the references and do not, therefore, include them on the title page, as a footnote to the title or otherwise. List here those individuals who provided help during the research (e.g., providing language help, writing assistance or proof reading the article, etc.).

### Nomenclature and units

Follow internationally accepted rules and conventions: use the international system of units (SI).
If other quantities are mentioned, give their equivalent in SI.

### Math formulae

Present simple formulae in the line of normal text where possible and use the solidus (/) instead of a horizontal line for small fractional terms, e.g., X/Y. In principle, variables are to be presented in italics. Powers of e are often more conveniently denoted by exp. Number consecutively any equations that have to be displayed separately from the text (if referred to explicitly in the text).

### Footnotes

Footnotes should be used sparingly. Number them consecutively throughout the article, using superscript Arabic numbers. Many word processors build footnotes into the text, and this feature may be used. Should this not be the case, indicate the position of footnotes in the text and present the footnotes themselves separately at

the end of the article. Do not include footnotes in the Reference list.

### Table footnotes

Indicate each footnote in a table with a superscript lowercase letter.

### Tables

Number tables consecutively in accordance with their appearance in the text. Place footnotes to tables below the table body and indicate them with superscript lowercase letters. Avoid vertical rules. Be sparing in the use of tables and ensure that the data presented in tables do not duplicate results described elsewhere in the article.

### References

*Citation in text*

Please ensure that every reference cited in the text is also present in the reference list (and *vice versa*). Any references cited in the abstract must be given in full. Unpublished results and personal communications are not recommended in the reference list, but may be mentioned in the text. If these references are included in the reference list they should follow the standard reference style of the journal and should include a substitution of the publication date with either 'Unpublished results' or 'Personal communication'. Citation of a reference as 'in press' implies that the item has been accepted for publication.

### Web references

As a minimum, the full URL should be given and the date when the reference was last accessed. Any further information, if known (DOI, author names, dates, reference to a source publication, etc.), should also be given. Web references can be listed separately (e.g., after the reference list) under a different heading if desired, or can be included in the reference list.

*References in a special issue*

Please ensure that the words 'this issue' are added to any references in the list (and any citations in the text) to other articles in the same Special Issue.

*Reference style*

*Text:* Indicate references by number(s) in square brackets in line with the text. The actual authors can be referred to, but the reference number(s) must always be given. Example: '..... as demonstrated [3,6]. Barnaby and Jones [8] obtained a different result ....'

*List:* Number the references (numbers in square brackets) in the list in the order in which they appear in the text.

*Examples:*

Reference to a journal publication:

[1] J. van der Geer, J.A.J. Hanraads, R.A. Lupton, The art of writing a scientific article, J. Sci. Commun. 163 (2010) 51–59.

Reference to a book:

[2] W. Strunk Jr., E.B. White, The Elements of Style, fourth ed., Longman, New York, 2000.

Reference to a chapter in an edited book:

[3] G.R. Mettam, L.B. Adams, How to prepare an electronic version of your article, In: B.S. Jones, R.Z. Smith (Eds.), Introduction to the Electronic Age, E-Publishing Inc., New York, 2009, pp. 281–304.

*Journal abbreviations source*

Journal names should be abbreviated according to the List of title word abbreviations http://www.sciencemag.org/site/feature/contribinfo/prep/res/journal_abbrevs.xhtml

**Submission checklist**

The following list will be useful during the final checking of an article prior to sending it to the journal for review. Please consult this Guide for Authors for further details of any item.

**Ensure that the following items are present:**

One author has been designated as the corresponding author with contact details:

• E-mail address

• Full postal address
• Phone numbers
• Keywords
Further considerations
• Manuscript has been 'spell-checked' and 'grammar-checked'
• References are in the correct format for this journal
• All references mentioned in the Reference list are cited in the text, and *vice versa*
• Permission has been obtained for use of copyrighted material from other sources (including the Web)
• Color figures are clearly marked as being intended for color reproduction

## AFTER ACCEPTANCE

### Proofs
One set of page proofs (as PDF files) will be sent by e-mail to the corresponding author (if we do not have an e-mail address then paper proofs will be sent by post). If there is any correction, please list your corrections quoting line number. If, for any reason, this is not possible, then mark the corrections and any other comments on a printout of your proof and return by fax, or scan the pages and e-mail, or by post. Please use this proof only for checking the typesetting, editing, completeness and correctness of the text, tables and figures. Significant changes to the article as accepted for publication will only be considered at this stage with permission from the Editor. We will do everything possible to get your article published quickly and accurately – please let us have all your corrections within 48 hours. It is important to ensure that all corrections are sent back to us in one communication: please check carefully before replying, as inclusion of any subsequent corrections cannot be guaranteed. Proofreading is solely your responsibility.

### Offprint
The corresponding author, at no cost, will be provided with a PDF file of the article *via* email (the PDF file is a watermarked version of the published article and includes a cover sheet with the journal cover image and a disclaimer outlining the terms and conditions of use). For an extra charge, paper offprints can be ordered via the offprint order form which is sent once the article is accepted for publication. Both corresponding and co-authors may order offprints at any time *via* e-mail (ajbse@ju.edu.sa)

## AUTHOR INQUIRIES

For inquiries relating to the submission of articles (including electronic submission) please visit this journal's homepage. Contact details for questions arising after acceptance of an article, especially those relating to proofs, will be provided by the publisher.

## DISCLAIMER

**Jouf Science and Engineering Journal** shall not take any responsibility for the contents of articles published in the journal and all such responsibility shall lie with the author/s. The opinions expressed in the articles are solely of the author/s and **JUSEJ** may not agree with such opinions in part or in full.

# METHODS TO ENHANCE THE SURGE MARGIN OF AXIAL FLOW COMPRESSORS AND PERFORMANCE OF A GAS TURBINE

## Ali H. Alnujaie[1], Mohammed Y. Tharwan[1], and Ahmed S. Hassan[1,*]

[1]Department of Mechanical Engineering, College of Engineering, Jazan University, P. O. Box 706, Jazan 45142, KSA

## *Corresponding author

## Ahmed S. Hassan

## Email address:

*ashassan@jazanu.edu.sa*

In the present study, a viscous nonlinear Moore-Greitzer equation model which could not control stall was used to construct a numerical simulation to control the surge, and the stall inside the axial flow compressor of gas turbine engines. Flow analysis and determination of rotational instability and surge within the axial compressor were performed to increase the compressor stable flow range and efficiency of gas turbines used for many purposes such as power generation, aircraft engines, missiles, etc. To suppress compressor rotary stall and surge, increase the stable running limit and improve gas turbine performance, the compressor inlet is injected with water in the air as one of the means to quell the instability process. Effect of inoculating 1% - 20% on stability of compressor and efficiency of gas turbines under different operating conditions was studied. The flow at which aerodynamic instability arising from rotational idling in compressors begins was determined using a simple model. A numerical analysis of contaminant emissions from gas turbine engine as a result of water injection was also conducted. An improvement was found in range of stable operation of compressor and performance of the gas turbines as well as the pollution emission rates.

| | | | |
|---|---|---|---|
| $A_c$ | Compressor area, m$^2$ | Q | Volumetric flow rate, m$^3$/s |
| $A_t$ | Throttle area, m$^2$ | r | Rotor radius, m |
| $\rho$ | Sound speed, m/s | s | Specific entropy, J/kgK |
| $C_x$ | Axial fluid velocity, m/s | T | Temperature, K |
| $T_{EG}$ | Temperature of exhaust gas, K | U | Rotor tip speed, m/s |
| H | Helmholtz frequency, Hertz | $V_p$ | Plenum volume, m$^3$ |
| Lc | Compressor length, m | $\upsilon$ | Specific volume of dry air, m$^3$/kg |
| $M_r$ | Mach number relative to the rotor | W/A | Water to air ratio by volume |
| $m_s$ | Surge flow rate with water spray | $\Omega$ | Specific enthalpy of vaporization for water |
| P | Pressure rise, kPa | $\omega$ | Mass of water vapor / dry air |
| $m_{so}$ | Surge flow rate without water spray | $\Phi$ | Flow coefficient, $= m_c / \rho\, A_c U^2$ |
| n | Amount of water inoculation/dry air | $\Psi$ | Pressure coefficient, $= \Delta P_c / 0.5 \rho u^2$ |

## 1.    INTRODUCTION

Axial flow compressors could be used in many engineering applications, including gas turbine engines, high-speed ship engines, power plants, blast furnaces, liquid catalytic cracking air, and propane dehydrogenation. And running it in unstable working conditions in many of these applications leads to the breakdown of all devices associated with it, so a lot of efforts are made to run it in stable conditions [1-8]. A rotary stall is an unsteady compressor operation condition in which the circumferential flow pattern is disturbed due to the formation of one or more low-flow stalled cells scattered around the compressor loop. The surge phenomenon is distinct as the incidence of robust variations in pressure and flow, escorted by a limited cycle, which leads to reversing the flow. The surge affects the entire compressor system. The deep type causes severe fluctuations in pressure and severe mechanical compressor damage. Operation of axial compressors in rotary stalling or surge leads to narrow operating ranges and causes deterioration in the performance of the gas turbine engine [9]. So far, many efforts were carried out to control the phenomena of unstable flow in axial compressors [10,11]. Also, many studies [12-17] have been done using different techniques to increase gas turbine performance. One of the most important is the injection of water or steam with air into the combustion chamber or at the inlet of the compressor. Effect of this injection on fuel consumption has been studied [1], on reducing NOx levels [3–9], and on power enhancement [10,11]. However, most researchers use simple thermodynamic models without taking into account the effects of water/steam injection on gas turbine performance or on the stable operation range [7-12]. With the recent developments of water spray technologies by cooling the air entering the compressor and its impact on performance of gas pipelines in both open and combined cycles [13] and its application to current engines, General Electric combined cooling the compressor inlet with water injection in the two-stroke engine LM6000 [14]. Some previous studies presented analytical or numerical methods that showed that injecting water into the compressor inlet at a rate of 12% of the base air volume [15-17] resulted in up to a 50% reduction in nitrogen oxide emissions. Some previous studies [18-21] presented analytical or numerical methods that showed that spraying the compressor inlet with water at a rate of 12% of the

base air volume has reduced NOx emissions by about 50%. Other researchers [22-32] showed in the laboratory that spraying water at 1% of the air volume has reduced compressor discharge temperature by 10%. Previous research has looked at effects of steam injection or water atomization at the compressor inlet on gas turbine performance. Nevertheless, links these effects to extent of compressor's stable working variety. The present work investigates effects of water injection at axial compressor inlet on gas turbine performance enhancement and reduction the NOx emissions.

## 2.    ANALYTICAL STUDIES

An analytical study was conducted to predict the effect of water injection into the compressor inlet at the start of the rotation stop. Details of the augmentation procedure can be found in [18, 26–34]. Also, Gretzer [28] developed a nonlinear model that captures the behavior of the limiting cycle after stopping in pressure systems. The non-dimensional model predicted the spinning increase or stop at the altitude line. Figure 1 shows a model for a gas turbine engine that consists of an inlet duct, a multistage axial flow compressor with an outlet duct, a combustion chamber, a turbine, and an exit throttle duct.
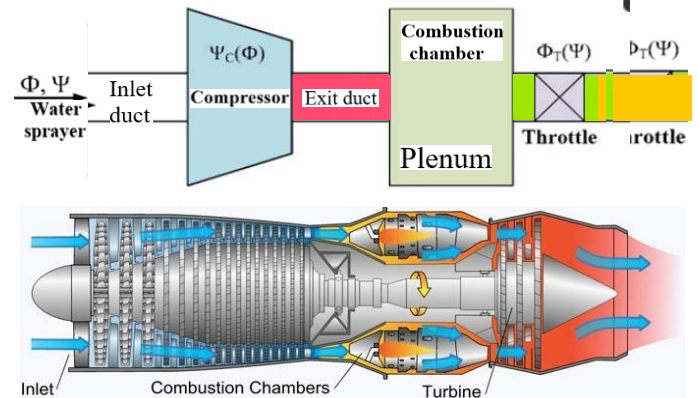


**Fig. 1.** The compression system and gas turbine model

### *2.1. EFFECT OF INCREASING AIR HUMIDITY ON COMPRESSOR PERFORMANCE*

To study the effect of inoculating water into air (increasing the density of the air as a result of increasing its humidity) at the inlet of the axial compressor on performance and the extent of stable work. The following equation can be written:

$$Tds_d = dh - \upsilon dp = h_a + \omega_* h_\upsilon + f_* h_l \qquad (1)$$

Where T is the temperature of the water droplet, $\upsilon$ is semi-perfect gas specific volume ($\upsilon = T(Ra + \omega Rv)/p$), and dh is the change in enthalpy

(dh=(dh=(c_{pa}+ ωc_{pυ}+fc_{pl})dT+Ωdω), f=4nπρ_lr²/3,  n water droplets number, and Ω water vaporization specific enthalpy. Equation (1) describes a non-stationary adiabatic flow. With no-slip and constant number of droplet conditions, thus:

$$dω/dt = − 4nπρ_lr²(dρ/dt) = (ρd_v/ρ)ln[(1+ω)/(1+ω_l)] \quad (2)$$

Where dω is specific humidity rise, dv diffusion coefficient, and ρ humid air density. Introducing Equ. (2) into Equ. (1) with definition of dh, gives:

$$dω = ω(1+ωM_a/M_v)[(Ω/TR_v)(dT/T) − dp/p] \quad (3)$$

The numerical integration of Equ. (3) Similar to [35], work inputs can be evaluated and represented in figure 2. The compressor required work as a function of water inoculation rate at different temperatures ranging from 10 to 50 °C is represented in the figure. Decrease in required power with an increase in water injection rate of up to 11% of dry air mass at different temperatures of the injected water is detected. That can be explained by decrease in the temperatures of air drawn into the compressor with increase in the rates of humidification of the air drawn. This is an excellent result that agrees with [35] numerical integration procedures and supports the validity of results. If the change in entropy is dsT, without velocity slip can be written as:

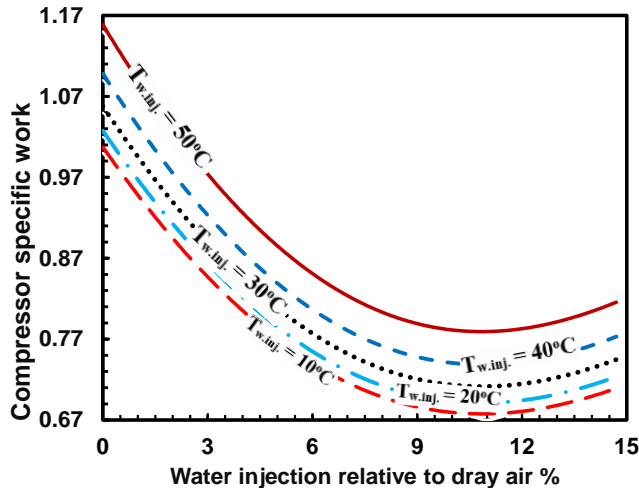$$ds_T = −4nπr²\{(Q/T_l)[(T−T_l)/T]+J[((h_v−h_l)/T_l)−(s_v−s_l)]\}dt \quad (4)$$



**Fig. 2**. Effect of water spray on compressor work

In case of saturated air, enthalpy increase is:

$$dh = (h_υ −h_l)∗dω + f∗c_{pl}dT_l+(c_{pa}+ ωc_{pυ})∗dT_l \quad (5)$$

Introducing Equ. (3) into Equ. (2) and incorporating Equ. (4) and (5), specific heat capacity c_p is:

$$C*_p=c_{pa}+ ωc_{pυ}+fc_{pl} +( 1+ωM_a/M_v)( ωL²/RT² ) \quad (6)$$

Using the Clausius-Clapeyron equation that can be written as:

$$d²P/dT²=(1/(υ_2− υ_1)\{[(c_{p2}−c_{p2})/T−2(α_2υ_2− α_1υ_1) dP/dT]+ k(T_2υ_2− T_1υ_1) d²P/dT²\} \quad (7)$$

In case of saturation, compensation from Equal. (5) in Equ. (7) for wet pressure work that calculated by numerical integration of Equ. (6), represented in figure 3. Examining figures 2 and 3 show that at a compression ratio of 8, evaporation rate decreases when spraying rate exceeds 9%. This is because, as rate of injection increases, rapid initial evaporation leads to lower subsequent temperatures.

The compressor aerodynamic performance is characterized by multi-directional efficiency, η_p, using increment dh from Equ. (5) is:

$$dh=vdp/η_p \quad (8)$$

The increase in static enthalpy across rotor blade is:

$$dh=0.5(1+ω+f)[V²_{x1}(1+tan²β_1) −U²_1−V²_{X2} (1+tan²β_2)+U²_2] \quad (9)$$

Where (1+ω+f) is constant factor, β relative flow angle. Figure 4 shows effect of water injection into an axial flow compressor on the rated turbine drive line. The transfer of operating points in the turbine's operating line to higher mass flow and compression ratio is evident. As water mist increases, the compressor characteristics become sharper and operating range decreases
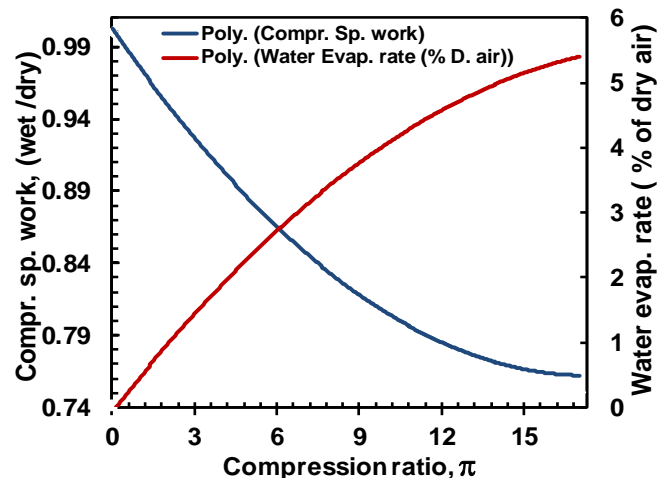


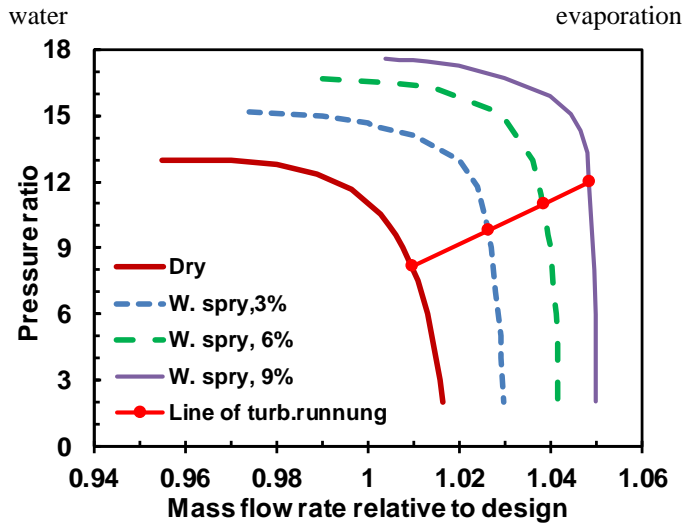**Fig. 3.** Effect of compressor pressure ratio on work and rate of

water                                                            evaporation



**Fig. 4**. Effect of water injection rate on compressor characteristics

## 3. ENHANCEMENT IN COMPRESSOR PERFORMANCE AND SURGE LIMIT BY WATER INJECTION

Referring to Figure 1, aerodynamic instability in gas turbine systems typically occurs near the optimum operating point for the compressor. This leads to serious consequences for the integrity of the entire system. The stop and surge onset can be inferred from the pressure system modeling analysis based on the experimental data of pressure rise versus flow rate. The dynamic stability limit can be derived from the maximum characteristic of the total pressure rise versus the static pressure. The cubic property of Gysling and Gretzer [35] and their model of axial flow compressors characterizing the dynamics of the pressure system were used in this paper

### 3.1. COMPRESSION SYSTEM GOVERNING FLOW EQUATIONS

The model shown in Fig. 1 consists of inlet duct, axial compressor, outlet duct, turbine, and control throttle at outlet. Suppose the dimensions of plenum are very large compared to dimensions of the compressor duct. Thus, the fluid velocity in the plenum chamber is small and the pressure is spatially uniform. The flow in compressor is incompressible, and gas inside the full chamber is compressible which acts as a gas spring. The pressure rise between the upper tank of compressor outlet duct and the base can be written as:

$$d\Psi/dt = \Psi c(\phi) - L_c(d\Phi/d\Psi) - m(d\varphi/d\zeta) - [2(d^2\varphi/d\eta d\zeta) + (d^2\varphi/d\eta d\theta)]/2 \qquad (10)$$

The mass balance equations for current model (Fig. 1) of local momentum equilibrium, and cyclic mean momentum equilibrium are:

$$d\Psi/dt = [\Phi + \Phi_w - \Phi_T(\Psi)]/(4B^2 L_c) \qquad (11\text{-}a)$$

$$d\Phi/dt = (Y/L_c)\{1 + (1.5 - 0.75J)[(\Phi/D) - 1][\Phi_w(\Psi_{co} - \Psi)/Y - 0.5[(\Phi/D) - 1]^3\} \qquad (11\text{-}b)$$

$$dJ/dt = J - J[(\Phi + \Phi_w)/D - 1]^2 - 0.25J^2 \qquad (11\text{-}c)$$

Where J is rotating stall squared amplitude, $L_c$ compressor channel nondimensional distance. Y, D compressor width and altitude. $\Phi$, $\Phi_W$, and $\Phi_T$ flow coefficient of compressor, water injection, and throttle. The compressor axisymmetric characteristic similar to Marco et al. [36], Mansoux et al. [37], and Peng et al. [38] is:

$$\Psi_c(\Phi) = 12.117\Phi^2 - 2.423\Phi + 0.221 \qquad (\Phi \le 0.1)$$

$$- 49.642\,\Phi^3 + 39.509\,\Phi^2 - 6.413\,\Phi + 0.395 \qquad (0.1 < \Phi \le 0.4)$$
$$\grave{}(12)$$

$$- 10.0695\,\Phi^2 + 9.430\,\Phi - 1.181 \qquad (\Phi > 0.4)$$

Figure 5 shows performance of a symmetrical compressor $\Psi c(\Phi)$ for stable and unstable operation conditions as well as throttle curve. It is noted that when throttle valve is closed slightly below compressor operating point (O.P.), the compressor becomes unstable. Equation (11-c) indicates that at dJ/dt =d$\Phi$/dt=d$\Psi$/dt= 0, the compressor is in stabile operation. Analyzing Equ. (10-c), at J(0)=0, shows the equilibrium values of unsteady perturbations of $\phi_o$, and $\psi_o$ given by intersection $\Psi_c(\Phi)$ and throttle curve.
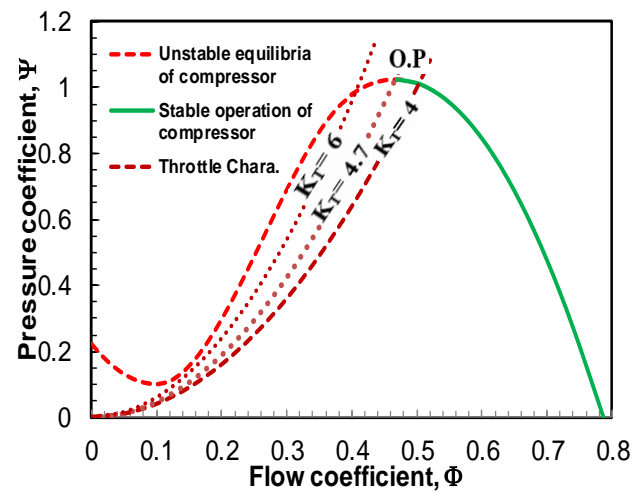


**Fig. 5.** *Steady and unsteady operation of an axial flow compressor*

At condition J(0) > 0 , dJ/dt = 0 fulfilled for J= 0, Equ. (11-c) becomes:

$$J = J_c = 4\{1 - [(\Phi + \Phi_w)/D - 1]^2 - [0.75D(\Phi + \Phi_w)/Y\gamma^2]\} \quad (13)$$

Introducing Equ. (12) into Equ. (11-b) and venue $d\Phi/dt = 0$, gives $d\Psi_{cs}(\phi)/dt$ gives:

$$\Psi_{cs}(\Phi) = \Psi_s(\Phi) + 5 \ \Psi(\Phi) - (8D/Y\gamma^2)[1 - D^2/(3 Y\gamma^2)]\Phi \ (14)$$

And the stall distinguishing is created at compressor characteristic as:

$$\Psi_s(\Phi) = \psi_{co} + Y\{1 - 1.5[((\Phi + \phi_\omega)/D) - 1] + 2.5[(\Phi + \phi_\omega)/D]^3\} \ (15)$$

The surge point, S, can be expressed [21] as:

$$S = [(m_d \pi_s/\pi_d m_s) - 1]*100\% \quad (16)$$

According to Gysling and Greitzer [35] derivation, Equs. (13 - 16), J = zero, surge cycle is:

$$d\Psi/dt = [\Phi - \Phi_T(\Psi)]/(4B^2 L_c) \quad (17\text{-}a)$$

$$d\Phi/dt = [(\Psi_c(\Phi) - (\Psi_T(\Phi) - \Psi]/L_c \quad (17\text{-}b)$$

From Equ. (17), a pair of ordinary differential equations for the annulus average of the axial momentum $\Phi(t)$ is:

$$\Psi(t) + L_c \, d\Phi(t)/dt = \int_0^{2\pi} \psi_c(\Phi)(t) + (\phi)_o)d\theta \quad (18)$$

Equations (16-18) show that the rotating stall transverse to the rotor tip is to be expected instead of following the stator. The reason for the occurrence of this phenomenon is the weakness of the energy carried by the fluid at the entrance of the stator, which leads to the rotation of the fluid or the termination of the flow in the passages of stator. This confirms that the rotating stall has developed in the space between the rotor and the stator and is the reason for the onset of the surge. Thus, this method establishes that the surge directly affects the performance characteristics of the compressor. To detect the initiation of rotating stall in the rotor over inviscid flow, the stagnation temperature and pressure relative to the inlet as a function of Mach number can be written similar to [28, and 29] as:

$$T_{o2w}/T_1 = [1 + 0.5(k-1)M_1{}^2](T_{2w}/T_1 - 1) + (k-1)M_1{}^2 \sin\beta_2 (W_2 - w_2)/U \quad (19)$$

$$\frac{P_{cew}}{P_i} = \left\{\left[1 + \frac{k-1)M_1{}^2}{2}\right. \right.$$
$$\left. + \left[\frac{1 + (w/U)^2 - 2(w/U)\sin\beta_2}{(T_{cew}/T_i) + [0.5(k-1)M_1{}^2]T_{cew}/T_i) - (w/U)^2)]}\right]\right\}^{(k-1)/k} \quad (20)$$

Where p is the pressure (N/m²), M is the Mach number.

## 3.2 EFFECT OF THE SPRAYING WATER ON THE AXIAL FLOW COMPRESSOR UNSTABLE OPERATION

Since what is required is to move the beginnings of the vortices to the left from the stable working state of the compressor, which is proportional to (S), the bifurcation curve slope at the operating point of the critical throttle position $(h_c)$, must be solved, and the following algebraic equation hangs on the unstable side of the bifurcation diagram:

$$\Phi_T = (\gamma\Phi_T + \phi + h) \ \Psi_T \quad (21\text{-}a)$$

$$\Psi_c(\Phi_c) = \Psi_p - 1.27S\partial^2[\Psi_{ci}(\Phi_c) + \Psi_c(\phi_w)]/\partial \Phi^2_c \quad (21\text{-}b)$$

$$\partial[[\Psi_{ci}(\Phi_c)]/\partial\Phi_c = -0.327S\partial^3[\Psi_{ci}(\Phi_c)) + \Psi_c(\phi_w)]/\partial^3\Phi_c \quad (21\text{-}c)$$

Differentiating Equ.21 in deference to (S), replaced the differentiation of Equs. (21-b, and c) into differentiation Equ (21-a), and explaining the result of the last algebraic shape for dS/dh, formerly figure critical of axial compressor operating $(h_c)$:

$$[\frac{dS}{dh}]_{h=h_c} = \Psi_P^{0.5}/[\frac{\gamma\frac{\partial\Psi_{ca}}{\partial\Phi_c} + \phi_w + 0.327\partial^3\Psi_c/\partial^3\Phi_c}{\partial^2\Psi_c/\partial^2\Phi_c} - \frac{\Phi_c}{2\Psi_c}\left(\gamma\Psi_{ca} - 0.125\frac{\partial^2\Psi_c}{\partial^2\Phi_c}\right)] \quad (22)$$

The nonlinear perturbation equations for the quantities, $\phi_c$, $\psi_c$, $\phi_T$, and $\psi_T$ in Equ. (2) was written in a matrix similar to [32], and then transformed the matrix into the following characteristic equation using Equs. (9, 10):

$$S^4 + a_3 S^3 + a_2 S^2 + a_1 S + a_o \quad (23)$$

The values of the complex growth rate can be dogged by solving Equ. (23) using the Mat lab, and deduce the result of the water injection on the instability margin. Figure 6 shows axial compressor mass flow relative to design (limit of stable operation of a minimum flow due to surge trigger and maximum flow due to choking), and pressure ratio relative to design at different engine speeds. Different percentages of water rates to air ratio were injected in the model at 0%, 5%, 8%, and 11%. The figure clearly shows good enhancements on the limits of stable operation and pressure rise. That is water injection has been works as feedback to suppress the surge trigger, and hence increases the pressure rise. The figure shows water-spray decrease flow rate which surge appears, up to 11%, mass for initiation surge occurs at higher flow rates.
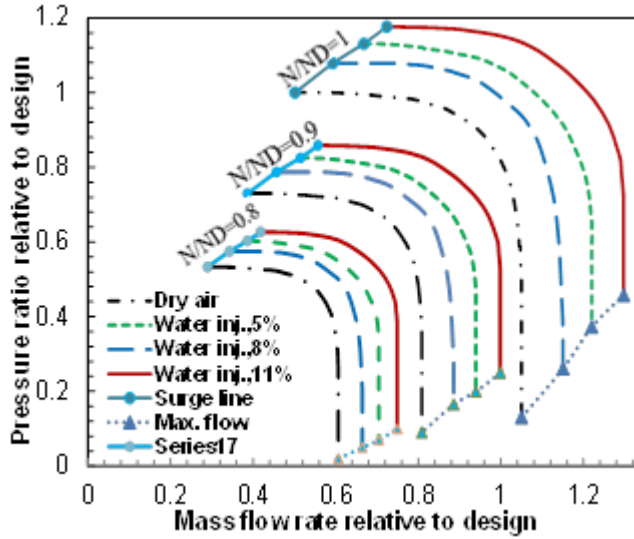
**Fig. 6.** Effect of water injection on compressor performance.

On other hand, applying ideal gas polytropic relations, exit temperature is:

$$T_{Oce} = T_{Oci} + (T_{Oci}/\eta_c)[(\pi_c)^{(k-1)/k}-1] \qquad (24)$$

And the compressor power is:

$$\dot{W}_c = (\dot{m}_a + \dot{m}_w)\,C_{pcavg}(T_{Oce}-T_{Oci}) = (\dot{m}_a+\dot{m}_w)[kR/(k-1)]T_i\{[(\pi_c)^{(k-1)/k}-1]/\eta_c\} \qquad (25)$$

where $T_{Oce}$, and $T_{Oci}$ are the stagnation temperature at the compressor exit and the system inlet, and $c_{pcavg}$ average wet air specific heat [39]. Combustion chamber exit pressure is $P_{cce} = P_{ce} - \Delta P_c$, and the temperature at gas turbine discharge, $T_{ote}$ using the turbine isentropic efficiency, $\eta_t$, is:

$$T_{ote} = T_{oti} - \eta_t T_{Oce}[1 - 1/(\pi_t)^{(k-1)/k}] \qquad (26)$$

Hereafter, if $\dot{m}_t$ $(=\dot{m}_a+\dot{m}_w+\dot{m}_f)$, the power produced from the turbine is:

$$\dot{W}_t = \dot{m}_t c_{pavg}(T_{Oti}-T_{ote}) = \dot{m}_t\,[kRT_{ote}/(k-1)][1-(\pi_t)^{(k-1)/k}]\eta_t \qquad (27)$$

Using Equs. (26 and 27), the gas turbine net generation power (kW) [40-42] is:

$$\dot{W}_{t\text{-}net} = (\dot{m}_a+\dot{m}_w+\dot{m}_f)w_t - (\dot{m}_a+\dot{m}_w)w_c - \dot{m}_f w_{bc} \qquad (28)$$

where $w_{bc}$ consumer power, gas turbine efficiency is:

$$\eta_t = \dot{W}_{t\text{-}net}/(\dot{m}_f LHV) \qquad (29)$$

Figure 7 shows compressor pressure ratio increases engine efficiency till 20, then constant this efficiency due to increases of the turbine power net power, while the gas turbine specific power (Kw/kg/s) has decreased by increasing the compressor pressure ratio due to decrease of turbine output power. Figure 8 shows effect of water injection on both enhancement of compressor surge limit, and gas turbine specific power (Kw/kg/s). The operating range of the induction

compressor increases with increasing water injection up to 10%, then decreases with increasing water injection. This is due to the decrease in the heat generated with an increase in the water content of more than 11% of dry air.

## 4.  EFFECT OF WATER INJECTION ON GAS TURBINE ENGINE PERFORMANCE AND EXHAUST GAS EMISSIONS

Many of the studies included in this paper concluded that adding a little water with the air drawn into the entrance of the gas turbine or injecting steam into the combustion chamber led to a decrease in exhaust gas temperatures and certainly reduces global warming. It also improved engine efficiency and reduced nitrogen oxides [1-7]. The mass of water inoculation (mw) and mass of gasoline (ma) can be estimated from the temperature drop owed to the enthalpy of the vaporization of water from the subsequent balance:

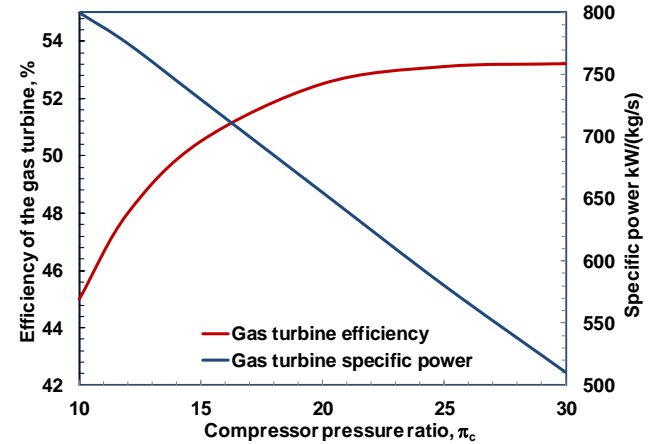$$m_m.\Delta h_m = m_m.Cp.\Delta T \qquad (30)$$



**Fig. 7**. Effect of compressor compression ratio on efficiency and specific power of gas turbine engine
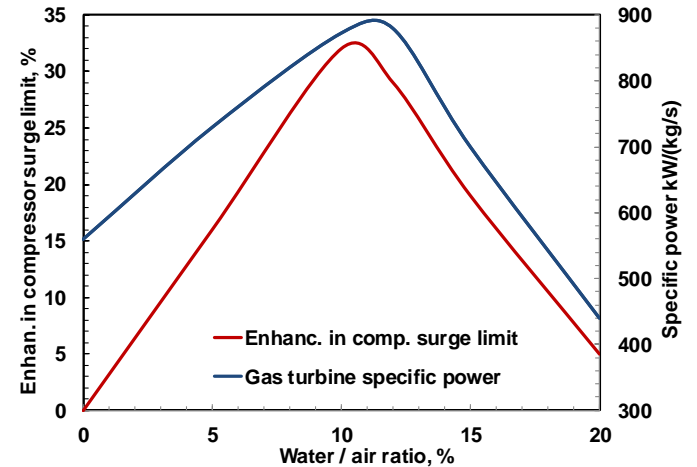


**Fig. 8**. Effect of water injection on compressor surge limit and gas turbine specific power

where $m_m$ is the water injection and $\Delta T$ temperature decrease. The wet compression work is calculated by adding the enthalpy changes of water vapour, dry air, and liquid water as:

$$(\dot{m}_a h_a + \dot{m}_g h_g)_1 + \dot{m}_{w1} h_{f1} + \omega_c = (\dot{m}_a h_a + \dot{m}_w h_w)_2 + \dot{m}_{w2} h_{f2} \quad (31)$$

The wet compression work ($\omega_c$) is:

$$\omega_c = C_{pa}(T_2 - T_1) + \omega_2(C_{pg} T_2 + h_{fg}) - \omega_1(C_{pv} T_1 + h_{fg}) + C_{pf} f_2 C_{pf} (T_2 - f_1 T_2) \quad (32)$$

Published by [44] was used to derive the following mass-conservation equation from, which can be used to evaluate the amount of evaporated water.

$$d\omega = (R_a / h_{fg})(T_2 - T_1)[(ln\pi_c / lnT_c) - \gamma/(\gamma-1) + (\eta_p - \gamma)/(\eta_p - 1)] \quad (33)$$

Where $T_c$ is the temperature ratio ($T_2/T_1$) and $\eta_p$ the polytropic compressor efficiency [45]. Figure 9 shows effect of decreasing the exhaust temperature with increasing the amount of water injection as a result of the decrease in the maximum temperature of the flame zone and the absorption of the latent heat of evaporation.
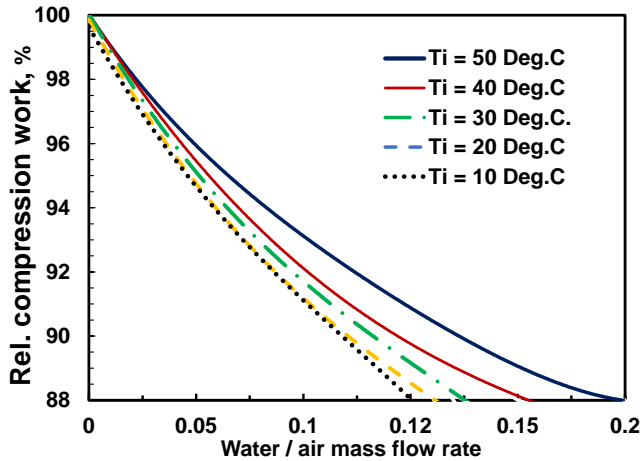


**Fig. 9.** Effect of water injection on gas turbine exhaust temperature

According to [23], the correlation equation with water injection can be written as:

$$\gamma[(1 - y)C_8 H_8 + yH_2 O] + [12.5(1 - y)][O_2 + 3.76N_2] = $$
$$C_8 H_8(\gamma - 1)(1 - y) + 8CO_2(1 - y)$$
$$+ H_2 O[\gamma y + 9(1 - y)$$
$$+ N_2[12.5(1 - y)] \quad (34)$$

And the proportion of burnt mass during the burning process can be written as:

$$\emptyset_b = \frac{mb}{m} = 1 - e^{ln(1.001)(\frac{\theta - \theta s}{\Delta \theta s})^n} \quad (35)$$

Where $\theta$ and $\theta_s$ are the specific internal energy for burned and unburned mixtures respectively. Figure 10 shows effect of water spray on NOx emissions (ppm). It is noted that

the percentage emission decreases with an increase in water spraying as a result of the lower engine temperature. Where emission of nitrogen oxides decreased by 25% at a rate of 20%. This is due to cooling prevailing in the combustion chamber due to the water not evaporating in the compressor. Thus, the water that does not evaporate in the combustion chamber suppresses the flame and leads to a decrease in the combustion efficiency and this result is consistent with [45].
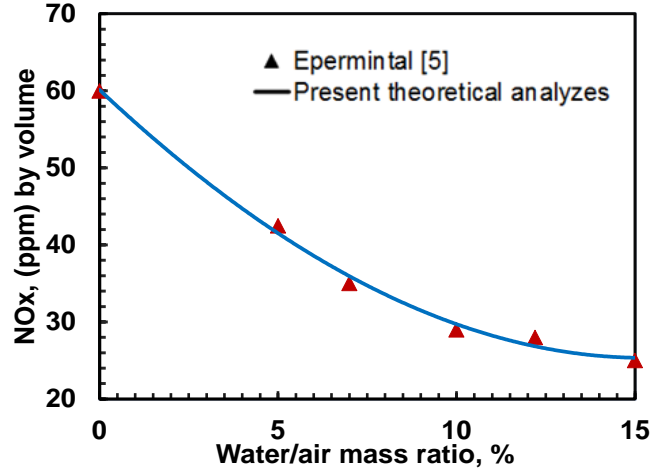


**Fig. 10.** Effect of water spraying on gas turbine emissions

## 5.    CONCLUSION

In this study, different analytical models of the flow through the gas turbine were implemented to reduce the exhaust gas emission and suppress the eruption by injecting different amounts of water with air at the inlet of the axial compressor. It was found that injecting water with the air entering the gas turbine resulted in reducing the energy required for the compressor by about 12%, the discharge gas emission by about 34%, and the reduction of nitrogen oxides by 35%. The higher decrease in NOx is attributed to the predominant cooling in the combustion chamber due to the water not evaporating in the compressor and reaching the combustion chamber to add additional energy to the engine and reduce the engine temperature. The results were compared with the experiments conducted by other researchers and the results showed that they are qualitatively acceptable

## 6. REFERENCES

[7] Ibrahem R. A., Effect of Molybdenum Disulfide Nano-particles on Dry Sliding Behavior of Carbon Fiber Reinforced Epoxy. Tribolgy in Industry, (2020) 115-120.

[8] Ibrahem R. A., Effect of Sunflower Seeds Husk and Peanut Shell Husk as well as Vegetable Oils on the Tribological Performance of Basalt Chopped Fiber Reinforced Epoxy Hybrid-Composites. Tribology In Industry, (2021) 624-631.

[9] Ibrahem R. A., and Samy A. M. ,TRIBOLOGICAL AND MECHANICAL PROPERTIES OF POLYMERIC. THE EGYPTIAN SOCIETY OF TRIBOLOGY, (2014) 53-62.

[10] Ibrahem R. A., Tribological performance of polyester composites reinforced with agricultural wastes. TribologyInternational, (2015), 463-466.

[11] Ibrahem, R. A., Effect of Date Palm Seeds on the Tribological Behaviour of Polyester. Material Science & Engineering, (2015) 1-5.

[12] Ibrahem, R. A., Influence of Natural Fillers on Tribological and. International Journal of Advanced Materials Research, (2016), 27-32.

[13] Ibrahem, R. A., Friction and Wear Behaviour of Fibre / Particles Reinforced Polyester Composites, International Journal of Advanced Materials Research, (2016), 22-26.

[14] Rahul K, Kausik K, Prasanta S, Sumit B, Study of mechanical properties of wood dust reinforced epoxy composite. ProcMaterSci.6, (2014), 551–556.

[15] Jesson D. A., Watts J. F., The interface and interphase in polymer matrix compo-sites: effect on mechanical properties and methods for identification. Polymer Rev 52, (2012), 321–354.

[16] Ali A. S., Ibrahem R. A., TRIBOELECTRIFICATION OF EPOXY REINFORCED by Aluminum mesh. THE EGYPTIAN SOCIETY OF TRIBOLOGY, (2019), 25-35.

[17] Rehab I. A., Mahmoud M. M., Mohamed A. T. and Ali W. Y., Increasing the Safety of Walking against Epoxy Floorings Reinforced by Metallic Wires", KGK, 05 (2016), pp. 54 – 59.

[18] El-Sherbiny Y. M., Samy A. M. and Ali W. Y., Electric Static Charge Generated from Bare Foot and Footwear Sliding Against Flooring Materials",

Journal of the Egyptian Society of Tribology, Vol. 11, No. 1, January (2014), pp. 1 – 11.

[19] Greason W. D., Investigation of a Test Methodology for Triboelectrification", Journal of Electrostatics, 49, (2000), 245 - 256.

[20] Diaz AF, Felix-Navarro RM. A Semi-Quantitative triboelectric Series for Polymeric Materials", Journal of Electric statics, 62, (2004) 277 - 290.

[21] Elhabib O. A., Mohamed M. K., AlKattan A. A. and Ali W. Y. Triboelectrification of Flooring Polymeric Materials", International Journal of Scientific & Engineering Research, Volume 5, Issue 6, June (2014) , pp. 248 - 253.

[22] Ali A. S., A. W., EFFECT OF BLENDING POLYETHYLENE TURF BY POLYMETHYL METHACRYLATE AND POLYAMIDE ON GENERATION OF ELECTROSTATIC CHARGE. THE EGYPTIAN SOCIETY OF TRIBOLOGY, (2020) 50-60.

[23] Morales H. M., Peppelman M., Zeng X., van Erp P. E.J., Van Der Heide E. Tribological behavior of skin equivalents and ex-vivo human skin against the material components of artificial turf in sliding contact", Tribology International, 102, (2016) 103 – 113.

[24] Ali A. S. and Ali W. Y. and Samy A. M., Electrostatic Charge Generated from Sliding on Polyethylene Turf", Journal of the Egyptian Society of Tribology, Vol. 17, No. 1 (2020), pp. 1 - 13.

[25] Ali A. S., A. W., SLIDING OF POLYETHYLENE COMPOSITES ON ARTIFICIAL TURF. THE EGYPTIAN SOCIETY OF TRIBOLOGY, (2020) 12-22.

[26] R. A. Ibrahem. Triboelectrification of Kapton Film under different Contact Modes. KGK- rubber point, (2021), 56-60.

[27] Zhong Lin Wang, Long Lin, Jun Chen, Simiao Niu, Yunlong Zi, Triboelectric Nanogenerators, book, (2016). DOI 10.1007/978-3-319-40039-6

[28] Meurig W. Williams, Triboelectric charging of insulating polymers–some new Perspective, AIP Advances 2, 010701; (2012) https://doi. org/10.1063/1.3687233

[29] J.A. Malecki, Physical Review B 59 (1999) 9954.

[30] B.C. Ten, J.H. Lang, IEEE Transcations on Circuits and Systems I: Regular Papers (2006) 53-288.

[31] F. R. Fan, et al., Flexible triboelectric generator, Nano Energy, (2012) doi:10.1016/j.nanoen. 2012.01.004

[32] J. Zhong, et al, Finger typing driven triboelectric nanogenerator and its use for instantaneously lighting up LEDs, Nano Energy, (2012) http://dx.doi.org/10.1016/j.nanoen. 2012.11.015

[33] Hulin Zhang, Ya Yang, Xiandai Zhong, Yuanjie Su, Yusheng Zhou, Chenguo Hu, and Zhong Lin Wang. Single-Electrode-Based Rotating Triboelectric Nanogenerator for Harvesting Energy from Tires ACS Nano 8 (1), (2014), 680-689 DOI: 10.1021/nn4053292

[34] Pengfei Zhao, Navneet Soin, Kovur Prashanthi, Jinkai Chen, Shurong Dong, Erping Zhou, Zhigang Zhu, Anand Arcot Narasimulu, Carlo D. Montemagno, Liyang Yu, and Jikui Luo., Emulsion Electrospinning of Polytetrafluoroethylene (PTFE) Nanofibrous Membranes for High-Performance Triboelectric Nanogenerators. ACS Applied Materials & Interfaces 10 (6), (2018) 5880- 5891. DOI: 10.1021/acsami.7b18442

[35] Jianxiong Zhu, Feng Ma, Hua Zhu., Single-Electrode, Nylon-Fiber-Enhanced Polytetrafluoroethylene Electret Film with Hollow Cylinder Structure for Mechanical Energy Harvesting. Energy Technology (6), (2018), 1112-1118. DOI. 10.1002/ente.201700779.

[36] Chi Zhang, Zhong Lin Wang. Triboelectric Nanogenerators. (2018) 1335z-1376. DOI: 10.1007/978-981-10-5945-2_38.

[37] Uddip K. and Sandip K. S., Enhanced Design of PPE Based on Electrostatic Principle to Eliminate Viruses (SARS-CoV-2)", Transactions of the Indian National Academy of Engineering, (2020) 1 – 6.

[38] Rachel Crowell., Electrified Fabric Could Zap the Coronavirus on Masks and Clothing, New materials and coatings could make fabric inactivate or repel viral particles, Biotech, June 24. (2020).

[39] Konda et al., Facemask Fabric Filtration Efficiency" Image courtesy of American Chemical Society, ACS Nano. (2020).

[40] Zhang R., Li Y., Zhang A. L., Wang Y. and Molina M. J., Identifying airborne transmission as the dominant route for the spread of COVID-19", Proceedings of the National Academy of Sciences. (2020).

[41] Ali A. S., Al-Kabbany A. M., Ali W. Y., Ibrahem R. A., Proper Material Selection of Medical safety goggles", Journal of the Egyptian Society of Tribology, Vol. 18, 2, (2020) 1 - 14.

[42] Wee-Jun Ong, Lling-Lling Tan, Yun Hau Ng, Siek-Ting Yong, and Siang-Piao Chai. Graphitic Carbon Nitride (g-C3N4)-Based Photocatalysts for Artificial Photosynthesis and Environmental Remediation: Are We a Step Closer To Achieving Sustainability?, Chemical Reviews 116 (12), (2016), 7159-7329 DOI: 10.1021/acs.chemrev.6b00075

[43] Kamel Eid, Mostafa H. Sliem, Maryam Al-Ejji, Aboubakr M. Abdullah, Messaoud Harfouche, Rajender S. Varma Hierarchical Porous Carbon Nitride-Crumpled Nanosheet-Embedded Copper Single Atoms: An Efficient Catalyst for Carbon Monoxide Oxidation. ACS Applied Materials & Interfaces , 14 (36) , .(2022), 40749-40760. https://doi.org/10.1021/acsami.2c06782

[44] Hou, J.; Yang, C.; Wang, Z.; Zhou, W.; Jiao, S.; Zhu, H. Appl. Catal., B (2013), 142−143, 504−511.

[45] In Situ Construction of g C3N4/g C3N4 Metal-Free Heterojunction for Enhanced Visible-Light Photocatalysis Fan Dong, Zaiwang Zhao, Ting Xiong, Zilin Ni, Wendong Zhang, Yanjuan Sun, and Wing-Kei Hodx. ACS Appl. Mater. Interfaces 2013, 5, 11392−11401 DOI: doi.org/10.1021/am403653a

[46] Xinchen Wang, Siegfried Blechert, and Markus Antonietti, Polymeric Graphitic Carbon Nitride for Heterogeneous Photocatalysis ACS Catalysis 2 (8), (2012) 1596-1606 DOI: 10.1021/cs300240x

# NOISE ANALYSIS OF SUBWAY

**Mofareh Hassan Ghazwani[1], Chitransh Singh[2*], Mohd Azeem[2], M. L. Chandravanshi[2], Ali Alnujaie[1*]**

[1]Department of Mechanical Engineering, Jazan University, P.O. Box 114, Jazan, 45142, Saudi Arabia

[2]Department of Mechanical Engineering, Indian Institute of Technology (Indian School of Mines), Dhanbad- 826004, Jharkhand, India

## *Corresponding author

**Chitransh Singh; Ali Alnujaie**

## Email address:

madan@iitism.ac.in; a.alnajee@gmail.com

*Submission Date*:      *Jan. 24, 2023*
*Accepted Date:*      *Feb. 21, 2023*

Subways are usually underground paths often built in cosmopolitan cities to access different localities with the ease. These subways also plays an important role in controlling traffic and convenient for the thousands vehicles. However, often noise pollution creates a big headache for the pedestrians due to lack of sound absorption materials in the subway and long duration of reverberation time. The objective of this research is to measure the noise level and evaluate the reverberation time (RT60) inside the subway. Noise levels were monitored in a subway located at IIT(ISM) Dhanbad campus. This subway connects the IIT campus with the teacher's colony located on the other side of National Highway 18. While vehicles passes inside the subway, it induces echo due to reverberation. Moreover, due to meager sound absorbing capacity of the construction materials such cements and concerts resulted in the higher level of noise inside the subway for longer durations. Theoretical analysis was carried out to determine the reverberation time in the subway. The design of subway was replicated in Solidworks and simulation for noise data was done in COMSOL to obtain the noise levels and verify the values of reverberation time. The simulated noise levels were confirmed by experimental results. The obtained results were compared with WHO standards for human comfort. The results revealed higher noise levels than the specified standards for certain conditions.

*Keywords:* *Acoustic monitoring, Noise level, Reverberation time, subway*

## 1. INTRODUCTION

- Acoustic analysis has become an essential study which needs to be carried out for every subway under constructions and indeed it's a growing field considering need and comfort of the future smart cities. A.I. El-Sharkawy et al. [1] conducted an experiments on analysis of traffic noise at Jeddah Saudi Arabia. The objective of study was to understand the noise generation and its responses in terms of sound levels (dB). The induced traffic noise levels and its effects on pedestrians were assessed and noise pollution index introduced through correlated to reactions received from every individual responses. Kang et al. [2] developed a theoretical model to implement mathematical formulae and through computer simulation models. The authors compared the theoretical formulae and computer simulations by an empirical data using a physical scaled model. Zhure et al. [3] conducted a study on Ankara metro system for designing optimum acoustical noise levels using

different noise absorbing materials. The optimum noise level was obtained using computer simulations through different sets of materials in layers. The exact relationship between noise transmission and their reverberation time were noted for each acoustic materials. Jacob et al. [4] worked on the effect of multiple branches on sound propagation in long enclosures. Various acoustic parameters such as noise level in terms of sound pressure level, its attenuations of noise, initial decay time periods and the reverberation time for each materials were investigated through physical scaled model for this study. Liqiutong et al. [5] conducted number of tests in laboratory for understanding the ground-borne noise originate in from subway lines using partial coherence analyses data. The observation revealed that sound used to propagate from subway lines to the surrounding buildings as well. This ground borne noise was identified from the experimental data obtained through partial coherence study. Different types of noises clearly identified from each unique vehicle which created the nose and named as vibrating sources in the study. In the study, the frequency range 20-320 Hz was found dominated compared to other higher frequencies. This is usual as most of the internal combustions engines used to produce noise levels in these range of frequencies only. Vertical vibration was found dominated compared to horizontal vibration. Donguk et al. [6] did noise analysis of a subway in capital city and near capital city in Korea during peak commuter's time to have an estimation of daily noise exposure of the commuters. On 15 subway lines, noise measurement was done for a period of two hours, during morning and in evening. Sound level and frequency analysis results obtained were compared with results of human comfort standards. Though the results suggested that noise level was loud enough to caused noise induced hearing loss. Yao et al. [7] were given a task to carry a research on different noise levels exposure by pedestrians while traveling in Toronto city. The authors based on their findings cautioned that mass transit in a underground metro stations have high noise levels and pose a quite potential health hazards in long and my induce hearing loses if the issue is not addressed on time.

Measurements of noise levels were conducted for the durations of 2 to 4 minutes. The data of noise levels of inside the metro stations and and outside of the various transits system was carried out through a noise dosimeter. Findings suggested that mean average noise level was within the permissible noise levels, however, intermittent impulse noise with very high 90 dB to 100 dB cause the potential threat to the passengers as it risks the noise induced hearing loses in pedestrians who use the path frequently. Wang et al. [8] examined sound fields of extra-large spaces with volume greater than 125 km3 and absorption coefficient was less than 0.7. Attenuation of reverberant energy with increasing source receiver distance was examined and then validated with simulation results using image source method. A modified model that is based on first reflections from floor is made. Agostonkatal in [9] worked on sound analysis to detect faults and expressed in terms of sound pressure level. Presence of fault causes modulation which was detected due to sidebands in the frequency spectrum. Tamara et al. [10] modeled a noise level study for Ivanic grad railway station in Croatia. Noise results of the simulation using RMR method were compared with field test data under different conditions. In first condition the vehicle acceleration and deceleration was used for the data acquisition explicitly and neglecting intermediate situations. The results revealed that noise levels from RMR method differed with the field measurements being RMR on higher side. V Mohanan et al. [11] tested the noise and vibration levels through data measurements using noise levels of the underground metro system. The results of the study of noise levels in terms of dB and vibration amplitudes in (g) were observed more than the standard limits. The authors have identified the possible causes which resulted in causing higher noise and reverberation time made recommendations to minimize this noise levels. Donguk Lee et al. [12] carried out research on the noise levels of a subway during peak time of rush of pedestrians. The study included the acquisition of noise level data in the frequencies range up-to 20 kHz in 15 locations of the underground metro-station. The study confirmed that the interior noise levels were within the

permissible limits. Though, few suggestions were highlighted in the research which could be implemented for further minimizing the noise levels and reverberation time as well. Study of characteristics of sound in open and close areas such tunnel or subway has to carry out carefully as it may be noisy and uncomfortable for the commuters. The assessment of the propagation medium and surface properties of the materials used in constructions of such enclosures thus imperative. Since sound is a propagation of mechanical waves in a medium but its behavior is almost similar to that of electromagnetic waves and can be represented mathematically similar to these waves. The sound waves during propagation also reflected, scattered and even decreased in sound absorbing materials. The sound though generated at any point within the enclosures has basically consists of two parts. Frist is direct sound heard from source of generation and the second type of sound is indirectly reached after so many reflections known as reverberation which depends on the type of geometry and location of the source and receiver.

- This article is sectioned as follows. A brief introduction and literature survey is described in section first followed by some basic terms used in noise measurement and analyses. The section 2 presents a theoretical and simulation analysis of reverberation time of the subway considered in this analysis. The simulated and experimental noise analysis has been compared in section 3. The results and discussion are presented in section 4 followed by the conclusions is section 5 of the article.

### 1.1. ACOUSTIC PARAMETERS

There are some basic terms exclusively used in the noise analysis are delineated such as Intensity of Sound which is the measure of energy flow in the sound wave propagation per unit area in any given unit time. It is usually measured in terms of decibels (dB) unit. The intensity of sound is mathematically expressed as $10\log_{10} I/I_0$, where, I- intensity of the sound expressed in watts per meter and the $I_o$ - reference intensity (usually taken as 10-12 w/m2). There is a variation in the hear sensitivity of human air with respect different frequencies from 1 Hz to 20 kHz. Therefore type of

sounds such as perceived by human is considered as A-weightings sound in dB unit, which is a measure of sound in audible spectrum as per the sensitivity of human ear. Sudden explosion or high intensity sound as generated during airplane or rocket take off are C or Z weightings in with dB unit.

During measurement of sound from the instrument such as 2270 (B&K) noise analyzer, A term (LAeq) represents steady propagation of sound level for any given time period and has equivalent A-weighted sound level which has similar acoustical energy as perceived by the human ears.

Usually at the time of propagation of sound waves from it source, the sound energy is decreases due to continuously in air friction known as air absorption. This air frictional force usually varies with temperature, humidity, pressure and frequency of the source sound and the air conditions. Mathematically, this variable can be expressed by an exponential law: $(r)=E0\ e{-2mr}$, where 2m is energy absorption coefficient of air. The sound propagation intensity also depends on the roughness or smoothness of materials as fraction of incident sound energy is absorbed by the surface known as surface absorption and reflection. The reflecting surfaces in the enclosures with fixed sizes and if sound generated at particular points, during propagation of these sound waves incidents on the surface with some angles and deflected randomly in various of angles. It cause some diffusion of sound power intensity and rest reflected which resulted in decay of sound till it reaches to measuring instruments. Another term known as speech intelligibility which means words correctly identified by listener out of the total works spoken. Usually it depends on reverberation and simultaneously background noise levels if arises. This intangibility index is usually expressed in scale 0 and 1. For acoustical propagation of sound in a room, the speech intelligibility index must be greater than 0.5.

### 1.2. STANDARD NORMS FOR NOISE CONTROL

As per the standards set by World Health Organization (WHO). In India also in line with international standards, the central pollution board of India has fixed the standard norms for noise levels for various areas such as Industrial area, residential area, school premises

and hospital area and for silence zones. The summery of the permissible noise level are given in Table 1. Any variation of noise levels in higher side is declared as unsafe for human ears and may induce health problems if subjected for longer durations.

**Table 1.** *Noise Pollution Standards in India as per Central Pollution Control Board [13]*

| Area code | Category | Daytime limit (dB, A-weightings) | Nighttime limit (dB, A-weightings) |
|---|---|---|---|
| A | Industrial Area | 75 | 70 |
| B | Commercial Area | 65 | 55 |
| C | Residential Area | 55 | 45 |
| D | Silence Zone | 50 | 40 |

As per the standards, few reference values of noise levels are considered standards such as hearing threshold value is assumed as 0 dB, quiet conversation usually considered if the sound level is bellow 25dB. Comfortable sound level to happen within 40 dB to 60 dB. Any restaurant with higher than 70 dB is assumed as noisy. Intense street traffic has noise levels usually considered above 90 dB. The take-off Jet engine generates above 120 dB noise levels and often causes threshold of pain in ears.

## 2. ANALYSIS OF REVERBERATION TIME (RT60) OF SUBWAY

According to the definition of reverberation time, sound pressure level drops by 60dB after being reflected from an incident surface. A 3-D model of the subway as shown in Figure (1) was developed in Solid-Works software in order to simulate the reverberation time. Figure (1)-b and Figure 1-c represent the satellite view and inside view of the subway respectively.
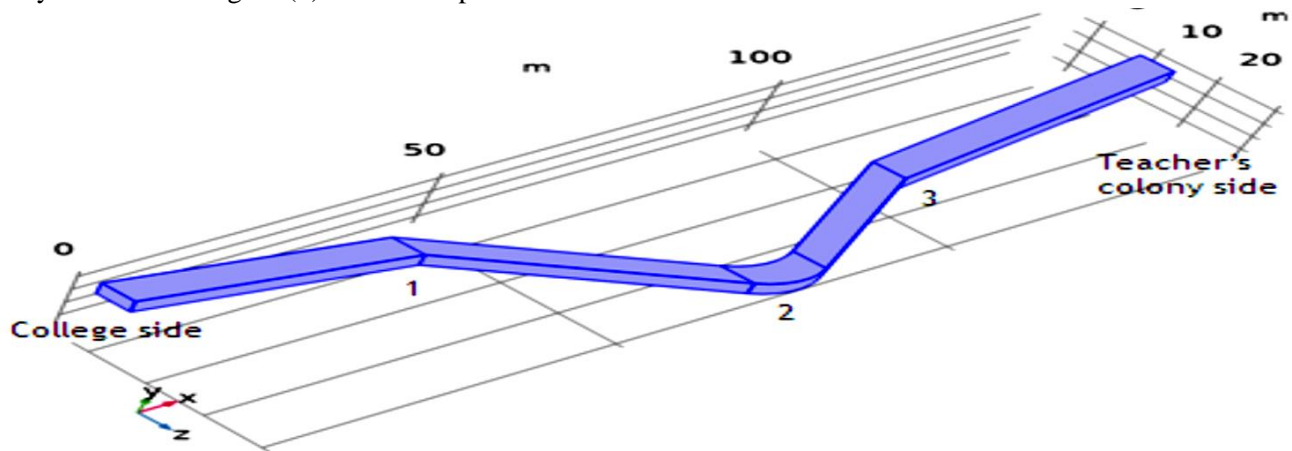


*(a). Dimension model of subway in SolidWorks*



*(b) Satellite view of subway in campus,    IIT(ISM) Dhanbad*

*(c)Cross-sectional view of subway with dimensions*

**Fig. 1.** Details of the sub-way.

### 2.1 THEORETICAL ANALYSIS

Theoretical analysis was carried out using Sabine equation and Eyring-Norris equation. The basic differences between these equations could easily understand by the following explanation given bellow:

**Table 2.** *Sabine equation and Eyring-Norris equations*

| Sabine Equation | Eyring -Norris equation |
|---|---|
| $(RT\ 60) = .613 * VA + 4mV$ | $(60) = -0.163 VS \ln(1-\alpha) + 4mV$ |
| Where, V is in $m^3$ volume of sound propagation | $\alpha$= average absorption coefficient |
| A= surface area in $m^2$ which absorb sound during propagation | V= total volume expressed in $m^3$ |
| $A = \alpha_1 S_1 + \alpha_2 S_2 + ............ \alpha_n S_n$ | S is the area of specific part |
| S is the area of specific part | Using the above equation we get, |
| A- absorption coefficient of the surface | |
| Thus RT(60)=1.612 seconds | RT(60) =1.6246 seconds |

The sound wave absorption coefficient (α) of surface depends on constructions of materials of walls. For example, a rough concrete absorption coefficient is 0.12 and for ceramic material tiles with very high surface finishing, its value is approximately 0.05.

The theoretical equations as summarized in Table (1) are used for estimation of reverberation time mathematically for the subway taken for current study. The value of reverberation time obtained from the theoretical analysis is approx. 1.612 s and 1.625s respectively from both methods. Further, to verify these values, simulation conducted of the 3D subway model and analyzed in COMSOL software, the details are given as follow:

### 2.2. SIMULATION ANALYSIS

The geometric properties of the subway obtained using COMSOL are shown in table (3).

The reverberation time found out in COMSOL using Sabine equation and Eyring-Noris equation are depicted in Figure 2 (a) and Figure 2 (b) respectively.

**Table 3.** *Geometric properties of the subway.*

| Sabine Equation | Eyring -Norris equation |
|---|---|
| Volume | 3270 $m^3$ |
| Surface Area | 3010 $m^2$ |
| Total room absorption area | 341.82 $m^2$ |
| Schroeder frequency | 43.42 Hz |
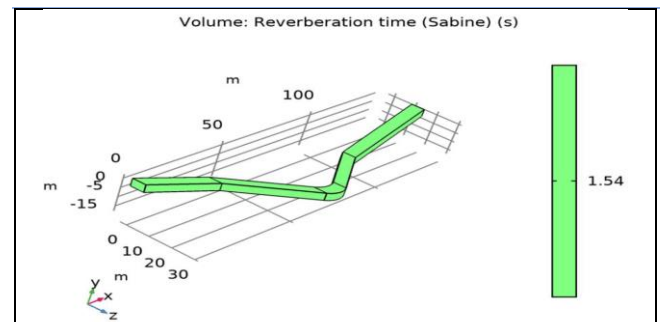


*(a). R.T using Sabine equation*
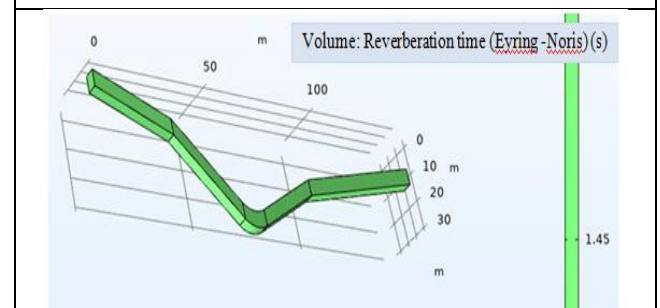


*(b). R.T using Eyring-Norris equation*

**Fig. 2.** Reverberation time (seconds) using Sabine and Eyring –Norris equation

It can be seen that the reverberation time using Sabine equation is 1.54 second, whereas by using Eyring-Norris equation is 1.45 second, which is in line with the theoretical values with marginal difference.

Since the subway has an area of over 3000m², thus the reverberation time of 1.6 seconds is acceptable, but it might lead to loss of speech intelligibility and cause irritation to the pedestrians. Further, noise prorogation

pattern is analyzed in subway using noise simulation and through experimental measurements as follows.
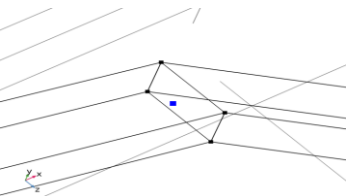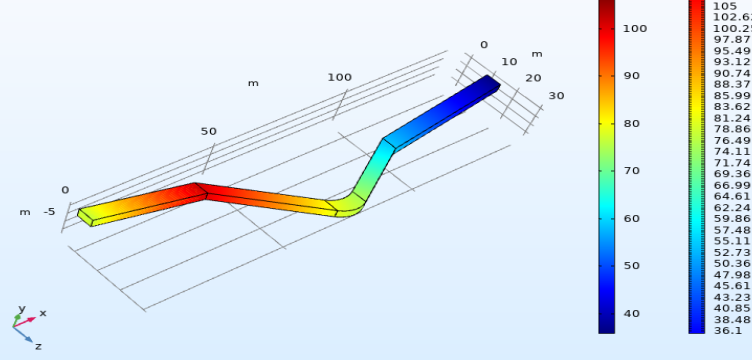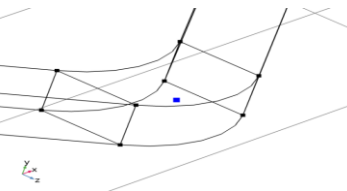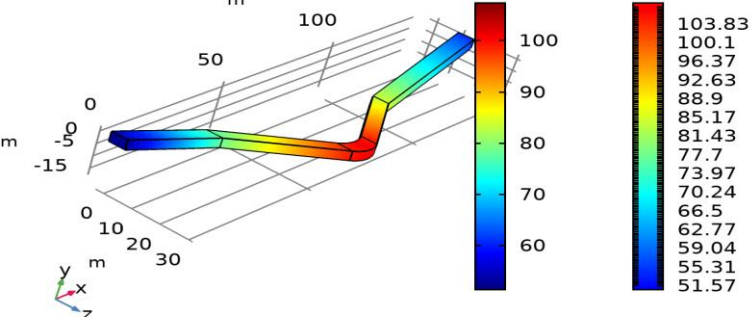
## 3. NOISE PROPAGATION ANALYSIS

Noise propagation analysis was carried out in COMSOL and the experimental data have also been acquired to observe the noise levels at various points on the subway and to determine the effects of prolonged exposure of this noise to humans.

### 3.1 NOISE ANALYSIS ON COMSOL

A model of subway was prepared in Solid-Works and imported in COMSOL. A point source of 0.3 Watts noise was generated at each of the three turn one after the other. The maximum noise level in decibels was determined. Table (4) depicts the simulated noise data for each case.

*Table 4. Simulated Noise data for noise source at each turn*

| S. No. | Condition | Noise level |
|---|---|---|
| 1. | **Point source at first turn**  **(a)** |  **(b)** |
| 2. | *Point source at second turn*  **(c)** |  **(d)** |

(e)

(f)
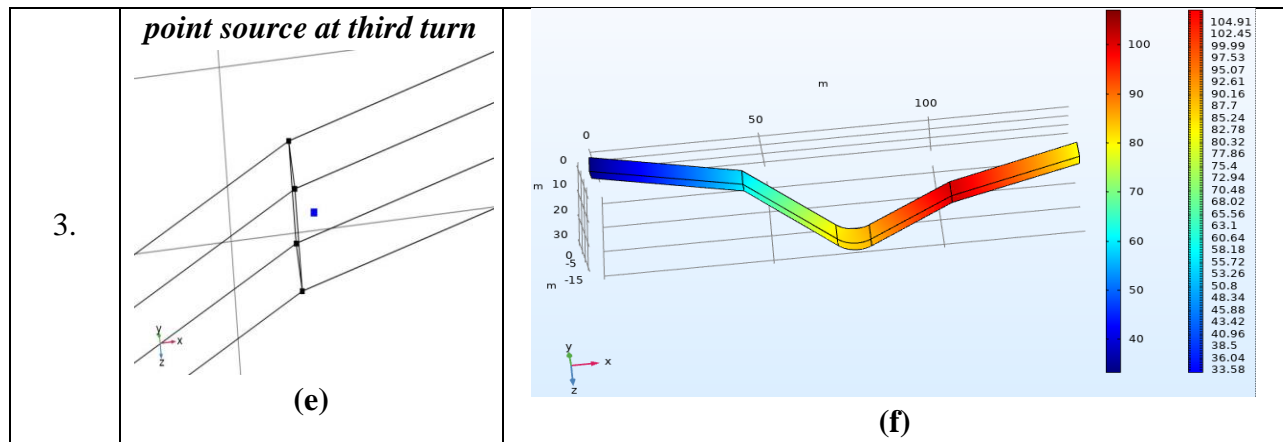
From the observation of the results as shown in Table (4), it is revealed that the noise level is very high on each turn. Such high noise levels can be harmful to the human ear. To obtain proper insights into the noise levels and to understand the response of human ear to this induced noise level due to vehicles, experimental noise study was conducted using 2 channel hand held noise analyzer (type 2270) as shown in figure (3).



**Fig. 3.** Hand held noise analyzer (2270) from (B&K)

### 3.2 EXPERIMENTAL NOISE ANALYSIS

Experiments were conducted to record and analyze the maximum as well as the equivalent noise levels. During the observations, the noise analyzer was kept at each of the three turns for a duration of 15 minutes at peak travel time between the two subway ends successively. The frequency range was kept within human hearing range of 20 Hz-20 kHz. The LZ as well as LA noise levels have been recorded and analyzed. The Z-weighing indicates unweighted frequency distribution. This distribution represents the actual noise level and is used for measurement of
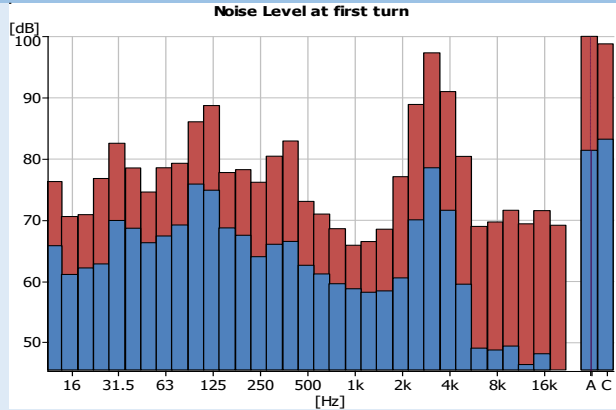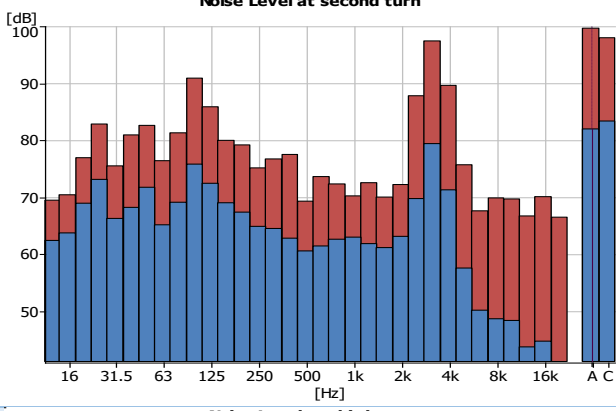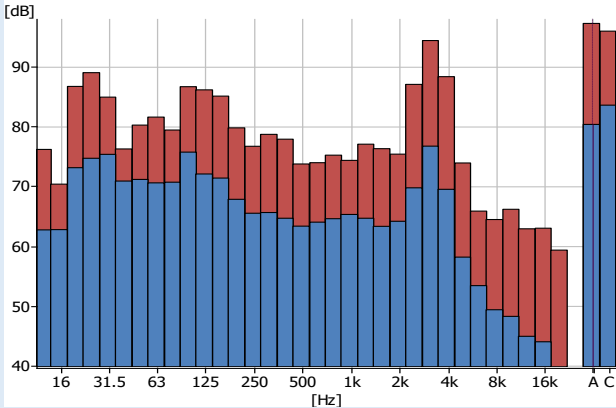
environmental noise. The A-weighing adjusts the sound pressure levels to reflect the sensitivity of human ear to noise

Real time data in one-third octave band was recorded and later analyzed to get the spectra in terms of equivalent noise level.

## 4.     RESULTS AND DISCUSSION

The data obtained from the experimental values of noise levels for A-weighted and Z-weighted frequency distributions are shown in table (5) and table (6) respectively.

**Table 5.** *Experimental Noise Levels in dB (A-weighing)*

| Subway turn no. | $LA_{eq}$ | $LAF_{max}$ | Spectrum | | |
|---|---|---|---|---|---|
| 1. | 81.3 | 100 |  Noise Level at first turn | | Cursor values<br>LAFmax: 100 dB<br>LAeq: 81.3 dB |
| 2. | 82 | 99.7 |  Noise Level at second turn | | Cursor values<br>LAFmax: 99.7 dB<br>LAeq: 82.0 dB |
| 3. | 80.3 | 97.2 |  Noise Level at third turn | | Cursor values<br>LAFmax: 97.2 dB<br>LAeq: 80.3 dB |

It can be perceived from table (5) that the maximum noise levels are in line with the simulated noise levels. Moreover, the A-weighted noise levels are higher than the accepted limits.

The Z-weighted noise levels and the respective spectrum is shown in table (6).

**Table 6.** *Experimental Noise Levels in dB (Z-weighing)*
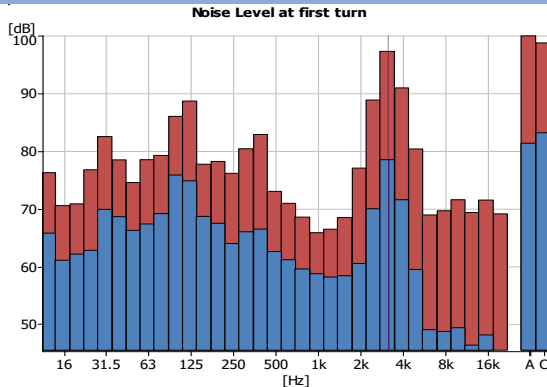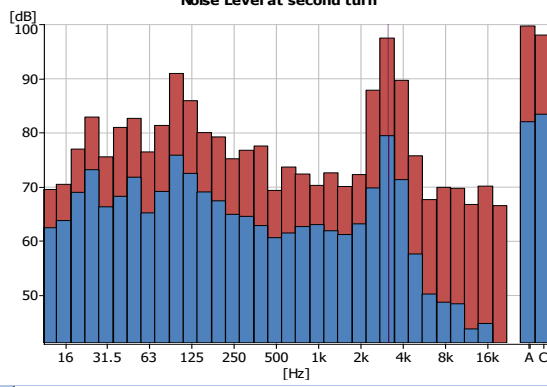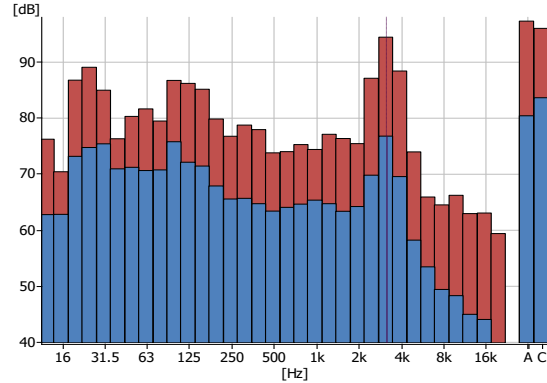
| Subway turn no. | $LZ_{eq}$ | $LZF_{max}$ | Spectrum |
|---|---|---|---|
| 1. | 78.5 | 97.3 |  |
| 2. | 79.4 | 97.4 |  |
| 3. | 76.7 | 94.4 |  |

Table (6) demonstrates that the Z-weighted noise levels are also higher than the acceptable limits. Also, the most dominant frequency is 3.15 kHz which is within the human hearing range. Due to the dominant component of noise being on higher frequency range, the noise will be sharp and impinging to the human ear causing uncomfortable conditions.

### 4.1 COMPARATIVE ANALYSIS

A comparison between the noise levels at each measurement point and the comparison of maximum A-weighted noise levels with the simulated noise levels and Indian Noise standards have been shown in Figure (4)-a and Figure (4)-b respectively.
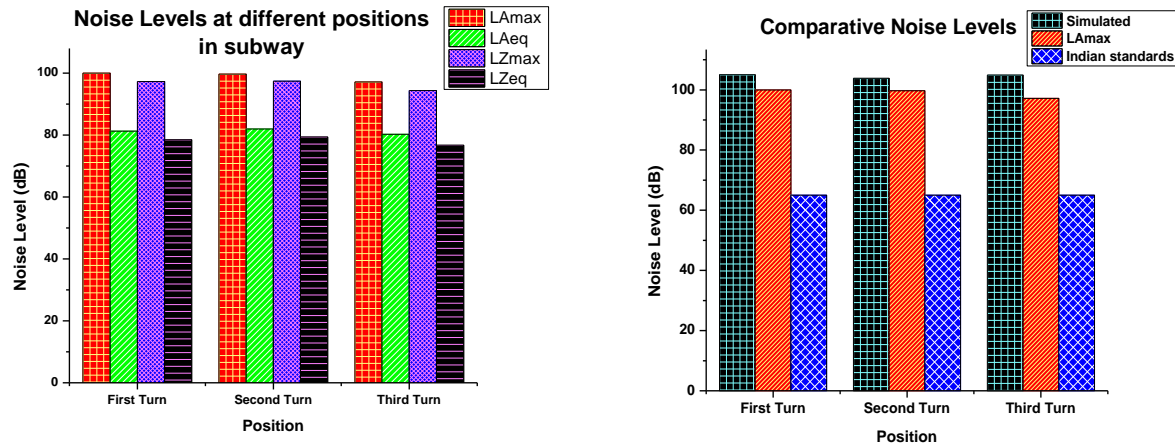


(a) Noise levels at different positions in subway

(b) Comparison of simulated and experimental noise levels with Indian standards

**Fig. 4.** A comparison between the noise levels.

The observations of the Figure (4) revealed that the equivalent noise levels recorded in the subway are above the acceptable limit prescribed by Indian standards. This implies that the pedestrians and the passengers in other vehicles will be affected. This will lead to low speech intelligibility, annoyance and even some temporary or permanent damage to the ear is possible.

## 5. CONCLUSIONS

This study was focused on determining the noise levels and reverberation time inside a subway connecting IIT (ISM) campus to the staff residence. The theoretical and simulated reverberation time was found to have quite similar values and differences were found within the accepted limit. Simulated noise levels were compared with experimental results. These results of noise levels revealed good co-relation between the simulated and experimental data. To determine the response of human ear to the noise levels, dB(A) weighted readings were also recorded and compared to the standards established by the government. The values of sound level were found on the higher side which may cause pain, irritation or damage to the human ear. However, this noise level generated for very short period of time and hence any possible damage can be nullified with minor precautions such as use of sound absorbing materials inside the subway and not blowing excessive horn. This will also help to improve the speech intelligibility inside the subway. Further, it can be concluded that use of sound absorbent materials during construction of subways or tunnels will be a good step towards reduction of environmental noise.

## 6. REFERENCES:

[1]  El-Sharkawy, A. I., and A. A. Aboukhashaba, "Traffic noise measurement and analysis in Jeddah" applied acoustics 16, volume 1 (1983): 41-49.

[2]  Kang, Jian "A method for predicting acoustic indices in long enclosures", Applied Acoustics

51, volume 2 (1997): 169-180.

[3]    Sü, Zühre, and Mehmet Çalışkan, "Acoustical design and noise control in metro stations: case studies of the Ankara metro system" Building Acoustics 14, no. 3 (2007): 203-221.

[4]    Liu, Jacob Chia-chun, and Po-Chien Lu, "Study on sound propagation in long enclosures with a vertical or inclined branch of different dimensions" Applied acoustics 70, no. 3 (2009): 522-529

[5]    Li, Qiutong, Y. Luo, and Y. Liu, "Experimental research on identification of ground-borne noise from subway lines based on partial coherence analysis" Procedia engineering 144 (2016): 1150-1157

[6]    Lee, Donguk, Gibbeum Kim, and Woojae Han, "Analysis of Subway Interior Noise at Peak Commuter Time" Journal of audiology & otology 21, no. 2 (2017): 61.

[7]    Noise exposure while commuting in Toronto - a study of personal and public transportation in Toronto Christopher M.K.L. Yao1, Andrew K. Ma1, Sharon L. Cushing1,2 and Vincent Y.W. Lin(2017)1,3,4

[8]    Wang, Chao, Hui Ma, Yue Wu, and Jian Kang, "Characteristics and prediction of sound level in extra-large spaces" Applied Acoustics 134 (2018): 1-7.

[9]    Katalin, Ágoston "Studying noise measurement and analysis", Procedia Manufacturing 22 (2018): 533-538.

[10]   Džambas, Tamara, Stjepan Lakušić, and Vesna Dragčević, "Traffic noise analysis in railway station zones" Applied Acoustics 137 (2018): 27-32.

[11]   Mohanan, V., Sharma, O. and Singhal, S.P., A noise and vibration survey in an underground railway system, Applied Acoustics 28 (4) (1989): 263-275.

[12]   Lee, D., Kim, G. and Han, W., Analysis of Subway interior noise at peak commuter time, Journal of Audiology and Otology 21 (2) (2017): 61-65.

[13]   Guidelines for Noise & Vibrations, Metro Rail Transit system. Ministry of Railways, India (2015) https://rdso.indianrailways.gov.in/works/uploads/File/MetroRailTransit_N&V%20 Guidelines%20(1).pdf

# OIL SPILL SEPARATION FROM SEAWATER BY USING AGRICULTURE LEAVES

## Mohamed A. Mahmoud[1,*]

[1]Chemical Engineering Department, College of Engineering, Jazan University, Jazan, Saudi Arabia.

**\*Corresponding author**

## Mohamed A. Mahmoud

**Email address:**

*Momahmoud@jazanu.edu.sa*

In this study, *Ficus carica* leaves were evaluated as a natural sorbent for oil removal from seawater. Wettability and FTIR study were used to characterize *Ficus carica* leaves. The maximum sorbent capacity (1.18 g/g) of *Ficus carica* leaves was obtained at 3.5 min and a dose of 0.5 g sorbent at room temperature. The isothermal and kinetic results showed that the sorption system was consistent with the Redlich-Peterson model ($R^2= 0.9924$) and the pseudo-second-order kinetic model ($R^2= 0.9934$). In addition, the reusability of *Ficus carica* leaves was evaluated..

*Keywords:* *Oil spill; Ficus carica; Isotherm; Kinetics; Thermodynamics*

## 1. INTRODUCTION

Oil is one of the most important sources of energy, and the demand for it is increasing. The import and export of oil through the seas and oceans exposes the aquatic environment to oil pollution due to oil spills [1]. Oil pollution affects not only the economy but also many other aspects of life, and is therefore considered an obstacle to development and a destroyer of the animate and inanimate environment [1-3]. Oil and its derivatives pose a high toxicity risk because gases are released when the spilled oil particles evaporate or decompose, and oil, especially crude oil, includes other toxic gases such as hydrogen sulphide (H2S) and others [4,5]. The spilled oil affects factories and oil refineries due to the risk of fires or explosions, and especially threatens desalination plants as drinking water can mix with toxic hydrocarbons, leading to prolonged shutdown of these plants [6]. Oil pollution can be biologically controlled by various methods such as shut-offs, skimming, burning, and adsorption processes [7-11]. Various agricultural adsorbents such as wheat straw [12], rice husks [13], sugarcane [14], waste flax fiber [15], kapok [16], banana peels [17], cotton [18] and orange peel waste [19] are well suited for removing oil from seawater. In this work, *Ficus carica* leaves as biodegradable biomass were used as adsorbents for the removal of oil from seawater in a batch system. The experimental parameters of the adsorption system were determined. In addition, the results were investigated using kinetics and isotherm models. In addition, the reusability of *Ficus carica* leaves was investigated.

## 2. MATERIALS AND METHODS

### 2.1. MATERIALS

*Ficus carica* leaves were obtained from farms. The oil/seawater sorption system was prepared using seawater with a salinity of 3.5% and used motor oil with a density of 706 kg/m$^3$ (auto repair shops)

### 2.2. PREPARATION OF THE ADSORBING BIOMASS

The leaves of *Ficus carica* were washed and dried at 85°C. The dried leaves were cut into small pieces and characterized by contact angle and FTIR analysis.

## 2.3. METHODS

The oil/seawater sorption system was prepared by spilling 1.0 g of oil on the surface of 1 l of seawater in a glass vessel. 0.1 g of *Ficus carica* leaves were contacted with the oil/seawater sorption system under the following sorption conditions: sorption time (0.5-4.5 min), oil dose (0.2-0.8 g), biomass dose (0.1-0.7 g), and temperature variation (25-50 °C). When equilibrium was reached, the loaded sorbents were separated from the oil/seawater sorption system, dewatered for 5 min, and weighed. The sorbed water in the drained biomass was separated by drying the drained biomass samples at 85°C for 12 hours and then reweighing them. The tests were performed three times, and then the data are presented as "mean ± SD"/error bar.

The oil removal percent (R%) was determined by eqs:

*R%=(Weight of loaded biomass after drying-Inital weight of biomass )/(Inital weight of oil)×100*     *(1)*

Also, the equilibrium sorption capacity $q_e$ (g/g) of *Ficus carica* leaves can be determined by eq.:

$q_e$=*(Weight of lsorbed oil)/(Inital weight of biomass) (2)*

## 3. RESULTS AND DISCUSSION

### 3.1 CHARACTERIZATION

#### 3.1.1. FTIR ANALYSIS

The functional groups of *Ficus carica* leaves were determined by FTIR spectrum (Thermo Fisher Scientific, USA). In Fig.1, it was found that the band 3466 cm$^{-1}$ is belongs to the OH group while the band 2950 cm$^{-1}$ refers to the C-H group [20]. In addition, the bands 1738 cm−1 and 1533 cm−1 refer to the C=O group [21]. The groups of -C-H group and CH2 groups appear at 1380 cm$^{-1}$ [22]. The bands at 621 and 612 cm$^{-1}$ represent the ether C-O group [23]. While the C-O-C group appears at 1170–1132 cm$^{-1}$.
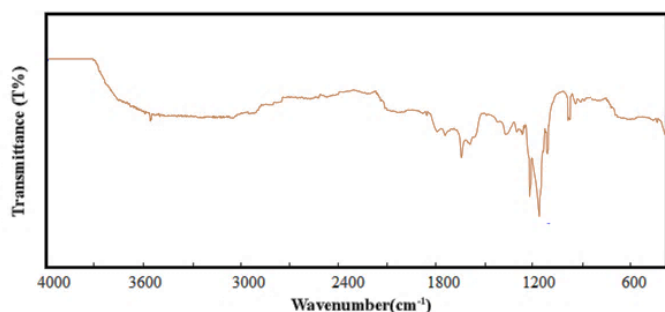


**Fig. 1.** FTIR analysis of *Ficus carica* leaves

Fig.2 shows the surface adhesion of oil and seawater on the leaves of *Ficus carica*. Fig.2a shows a high superficial adhesion (contact angle :15±2°) of oil on *Ficus carica* leaves. Fig.2b shows low superficial adhesion (contact angle :166±1°) of *Ficus carica* leaves with seawater which shows the lipophilic and hydrophobic nature of *Ficus carica* leaves that increases the oil sorption capacity of the biomass [15, 24].
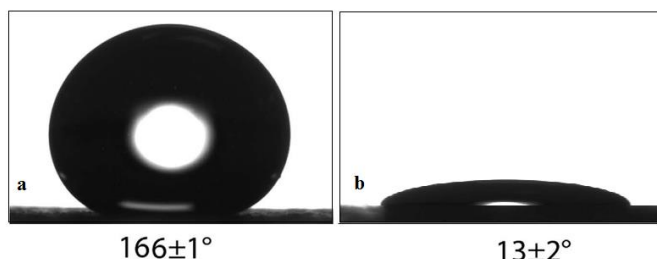


**Fig. 2.** Contact analysis of Ficus carica leaves with (a) water and (b) oil

## 3.2. SORPTION DYNAMICS

### 3.2.1. EFFECT OF SORPTION TIME

The effect of contact time was studied in the variation (0.5-4.5min) by interaction of 0.1g *Ficus carica* leaves on 0.5g oil / 1L seawater at 25°C in a glass vessel. Fig. 3a shows the sorption results and the maximum sorption capacity reached 1.18 g/g with a removal percentage of 70.75% after 3.5 min. The laboratory results show that the removal rate is fast in the first phase (0.5-3.5 minutes) due to the capillary adsorption force and the strong interaction of oil with the empty adsorption sites (Lim and Huang, 2007a,b). In contrast, after 3.5 minutes, there is no significant change in percent removal [25].
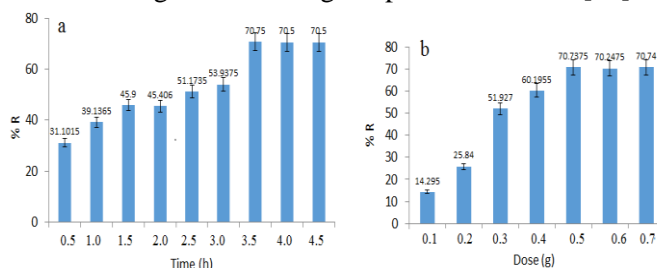


**Fig. 3.** Sorption time (a) sorbent dose (b) plots of oil onto *Ficus carica* leaves

### 3.2.2. EFFECT OF BIOMASS DOSE

The effect of the amount of adsorbent material in the adsorption process is important from an economic and operational point of view, because increasing the amount of adsorbent material above the required level means a loss of raw materials and an increase in the cost of their

separation after the adsorption process. In this work, the effect of adsorbent dose (0.1-0.7 g) on adsorption of spilled oil (0.5 g oil/1 l seawater) at 25 °C and 3.5 minutes was studied. Fig. 3b shows an increase in the percentage of oil removal from 14.29% to 70.73% when the amount of adsorbent is increased due to the availability of sorbent sites on *Ficus carica* leaves, then the percentage of oil removal is fixed [26]. These results indicate that the economic dose of adsorbent required to remove oil (0.5 g oil/1 l seawater) is 0.5 g *Ficus carica* leaves.

### 3.2.3. EFFECT OF THE OIL DOSE

Studying the effect of the amount of oil spilled on the water surface is very helpful in determining the oil removal factors and the efficiency (maximum sorption capacity) of the removal process. Therefore, the effect of different amounts of spilled oil (0.2-0.8 g) on the surface of seawater was studied using a fixed amount of adsorbent (0.5 g) at 25 °C and 3.5 minutes. Fig. 4a shows that the oil sorption capacity of *Ficus carica* leaves was increased from 0.74 to 1.18 g/g. While the removal percentage decreased from 46.65% to 70.75% with the increase of spilled oil from 0.2 to 0.4 g, which was due to the increase of spilled oil on the surfaces of *Ficus carica* leaves [27].
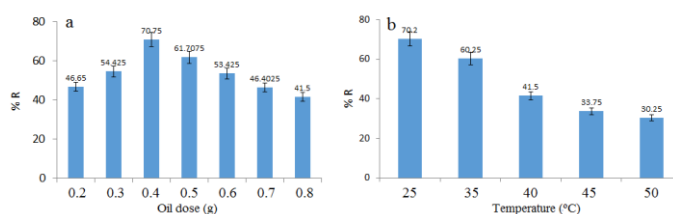


**Fig. 4.** Sorption dynamics: Oil concentration (a) sorption temperature (b) of oil sorption onto *Ficus carica* leaves.

### 3.2.4. TEMPERATURE EFFECT

Air temperature plays an important role in the removal of spilled oils, as it affects the degree and duration of oil adhesion (sorption) on the surface of *Ficus carica* leaves by changing the viscosity of spilled oils and the sorption power of the *Ficus carica* surface [13]. Fig. 4b shows the decrease in sorption capacity of *Ficus carica* leaves from 1.18g/g to 0.26g/g by changing the temperature from 25°C to 50°C. The decrease in sorption capacity of *Ficus carica* leaves is due to the decrease in oil viscosity with the increase in temperature, which increases the loss of sorbed oil from biomass due to the dehydration time [15].

### 3.3 KINETIC MODELING

Experimental results of *Ficus carica* leaves were studied by linear kinetic fitting with modeling results of pseudo-first-order, pseudo-second-order and Elovich kinetic models using the following equations:

Pseudo-first-order model [15, 16].

$$Log(q_e - q_t) = log k_1 q_e - k_1 t \tag{7}$$

Pseudo-second-order model [28].

$$\frac{1}{q_t} = \frac{1}{K_2 q_e^2} + \frac{1}{q_e} t \tag{8}$$

The *Elovich kinetic model* [15,20].

$$q_t = \frac{1}{\alpha} ln(\alpha\,\beta) + \frac{1}{\alpha} ln\,t \tag{9}$$

Where, qt and qe (g/g) are the capacity at time t. and equilibrium. $K_1$ (L/min) and $K_2$ (g/mg.min) are the constants of the pseudo-first order and pseudo-second order models, respectively. In addition, α and β the constants of the Elovich mode.

The kinetic fit was studied using the correlation factor ($R^2$) factor [15].

$$R^2 = \frac{(\sum_{i=1}^{n}(q_e\,experimental - q_e\,calculated)^2)}{\sum_{i=1}^{n}\sum_{i=1}^{n}(q_e\,experimental - q_e\,calculated)^2} \tag{10}$$

Table 1 shows the results of the kinetic models. The pseudo-second-order model shows agreement between the theoretical sorption capacity (1.33 g/g) and the experimental qe (1.18 g/g). Moreover, the value of $R^2$ indicates that the pseudo-second-order model (R2=0.9934) agrees well with the experimental results (Fig. 5), suggesting that the physiochemical interaction of oil on *Ficus carica* leaves.



**Fig. 5.** Pseudo-first-order (a) Pseudo-second-order (b) Elovich (c) kinetic models of used oil uptake onto *Ficus carica*

**Table 1:** *Sorption isotherm models*

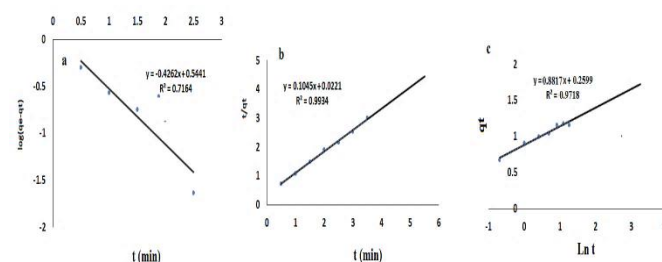| isotherm models | Equations | Parameters |
|---|---|---|
| **Langmuir** | $\dfrac{C_e}{q_e} = \dfrac{1}{K_L Q_L} + \dfrac{C_e}{Q_L}$ | $C_e$ (g/g): the oil concentration at equilibrium. $K_L$ (L/min) $Q_L$(g/g): Langmuir constants |
| **Freundlich** | $Log q_e = Log K_F + \dfrac{1}{n} Log C_e$ | $K_F$ (g/mg.min) and n : Freundlich constants |
| **Redlich-Peterson** | $Ln\,\dfrac{C_e}{q_e} = B\ln C_e - LnA$ | $A$ (L/g)$^\beta$ and $\beta$ : constants of Redlich-Peterson model. |

### 3.4 ISOTHERMAL MODELING

Three isotherms were used to study the mechanism of oil adsorption on *Ficus carica* leaves

Table 2 shows the isotherm models and their equations [18, 19]. Fig. 6 shows the pattern of isotherm models. The modeling results (Table 3) show good agreement with the Redlich-Peterson isotherm ($R^2$= 0.9924) compared to the other models, indicating that the interaction of the oil with the *Ficus carica* leaves is a monolayer sorption.
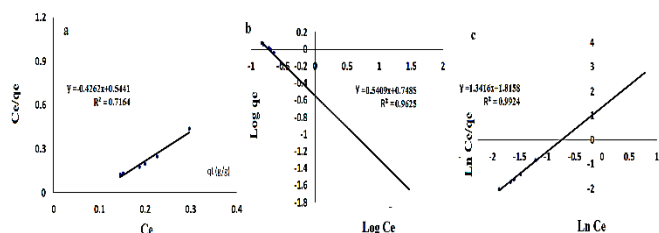


**Fig. 6.** Langmuir (a) Freundlich (b) Redlich-Peterson (c) isotherm models of used oil uptake onto *Ficus carica*.

**Table 2:** *Results of sorption kinetics*

| Kinetic model | Parameter | values |
|---|---|---|
| **Pseudo-first-order** | $q_e$(g/g) | 8.2127 |
| | $K_1$(L/min) | 0.4262 |
| | $R^2$ | 0.7164 |
| **Pseudo-second- order** | $q_e$(g/g) | 1.3333 |
| | $K_2$(g/mg.min) | 8.4331 |
| | $R^2$ | 0.9934 |
| **Elovich** | $\beta$ | 1.1839 |
| | $\alpha$ | 1.1341 |
| | $R^2$ | 0.9718 |

**Table 3:** *Results of sorption isotherm studies.*

| Isotherm model | Parameter | Value |
|---|---|---|
| **Langmuir isotherm** | $Q_L$(g oil/ g biomass) | 2.3463 |
| | $K_L$ (L/g) | 0.7833 |
| | $R^2$ | 0.7154 |
| **Freundlich isotherm** | $K_F$ (g $^{(1-1/n)}$ L$^{1/n}$g$^{-1}$) | 5.6027 |
| | n | 1.8487 |
| | $R^2$ | 0.9625 |
| **Redlich-Peterson isotherm** | B | 1.3416 |
| | $A$ (L./ g )$^\beta$ | 1.7060 |
| | $R^2$ | 0.9924 |

### 3.5 THERMODYNAMIC INVESTIGATION

Thermodynamic studies of oil reaction on *Ficus carica* leaves were investigated by determining the values of enthalpy ($\Delta H_o$), Free energy ($\Delta G_o$) and entropy ($\Delta S_o$) using the equations [29]:

$$\text{Free energy } (\Delta G) = -RT \log K_c \qquad (13)$$

$$\Delta G = \Delta H - T\Delta S \qquad (14)$$

$$Ln K_c = \Delta S/R - \Delta H/RT \qquad (15)$$

$$K_c = \text{Equilibrium sorption capacity/unsorbed oil (g/l)} \qquad (16)$$

Where R: gas constant and T: temperature (K) of the oil/seawater system. The results (Table 4) of the Van't Hoff plot (Fig. 7a) show that the free energy values decrease with increasing temperature, indicating that the efficiency of *Ficus carica* leaves decreases with increasing temperature. Moreover, the negative value of $\Delta H_o$ (-246.541 kJ.mol$^{-1}$) indicates the exothermic nature of oil sorption [30].
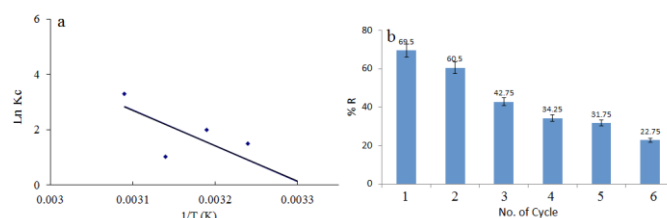


**Fig. 7.** Van't Hoff plot (a) and reusability cycles (b) of oil uptake onto *Ficus carica*

**Table 4:** *Thermodynamic sorption studies.*

| T (K) | $\Delta G$ (kJ.mol$^{-1}$) | $\Delta H$ (kJ.mol$^{-1}$) | $\Delta S$ (KJ.mol$^{-1}$.k$^{-1}$) |
|---|---|---|---|
| **298** | -10.763 | -246.541 | -0.761 |
| **308** | -12.153 | | |
| **313** | -8.348 | | |
| **323** | -o.262 | | |

### 3.6   REUSE STUDIES

The reuse of the adsorption material after the adsorption process is considered as one of the economic aspects of the oil adsorption process, because it saves the raw material and recovers the adsorbed oils. Therefore, it is important to study the reuse of loaded *Ficus carica* leaves and to know the effects of reuse cycles on the efficiency of the leaves.The loaded *Ficus carica* leaves were reused after the sorbed oils were separated and reused by squeezing and drying.

The percentage of desorbed oil (Do%) is determined by the equation:

$$D_o(\%) = \frac{(Weight\ of\ loaded\ biomass\ -\ Weight\ of\ biomass\ after\ \text{squeezing})}{Inital\ weight\ of\ oil} \times 100$$

Fig. 7b shows that the sorption efficiency of *Ficus carica* leaves decreases with increasing desorption cycles, which is due to a reduction in the sorption sites of *Ficus carica* leaves. Half the economic efficiency of *Ficus carica* leaves was achieved after five adsorption-desorption cycles. Table 5 shows the recycling efficiency of *Ficus carica* leaves and other biomass. The results show that *Ficus carica* leaves perform respectably in removing oil spills from seawater.

**Table 5:** *Evaluation of oil uptake of Ficus carica leaves with other biomasses.*

| Sorbent material | Sorption capacity (g/g) | Reference |
|---|---|---|
| **Flax fiber** | 13.75 | [15] |
| **Banana peel** | 6.35 | [17] |
| **sugarcane** | 11.3 | [14] |
| **Sawdust** | 6.4 | [7] |
| **Coir fiber** | 5.4 | [7] |
| **Sisal** | 6.4 | [7] |
| **kapok fiber** | 38.1 | [16] |
| *Ficus carica* | 1.18 | Present study |

### 4.   CONCLUSIONS

The potential of *Ficus carica* leaves as an oil-sorbing biomass in a seawater system was investigated. The oil/seawater batch system showed that the process is determined by the sorption parameters (contact time and sorbent dose, oil dose and temperature). In the exothermic system, the maximum oil capacity of *Ficus carica* leaves reached 1.18 g/g at 3.5 min and 0.5 g sorbent dose. In addition, the sorption results were investigated using kinetic and isothermal models. The pseudo-second-order kinetic model and the Redlich-Peterson model

fitted well with the experimental results. The surface and capillary sorption of *Ficus carica* leaves are the mechanism of oil sorption system. The reusability of *Ficus carica* leaves shows that the economic sorption capacity decreased after 5 reusable cycles

### 5.   REFERENCES

[1] S.E. Allan, B.W. Smith, K.A. Anderson, Impact of the deep-water horizon oil spill on bioavailable polycyclic aromatic hydrocarbons in Gulf of Mexico coastal waters, Environ. Sci. Technol. 46 (2012) 2033–2039.

[2] P.K. Andy Hong, T. Xiao, Treatment of oil spill water by ozonation and sand filtration, Chemosphere. 106 (2013) 460–467.

[3] M. Mojžiš, T. Bubeníková, M. Zachar, D. Kaˇcíková, J. Štefková, Comparison of natural and synthetic sorbents' efficiency at oil spill removal, Bio. Resources. 14 (2019) 8738–8752.

[4] H. Zhu, S. Qiu, W. Jiang, D. Wu, C. Zhang, Evaluation of electrospun polyvinyl chloride/polystyrene fibers as sorbent materials for oil spill cleanup, Environ. Sci. Technol. 45 (2011) 4527–451.3

[5] A. B.Olabintan,E. Ahmed,H.Al Abdulgader,T. A.Saleh, Hydrophobic and oleophilic amine-functionalised graphene/polyethylene nanocomposite for oil–water separation, Environmental Technology & Innovation 27(2022)102391.

[6] J.C. Onwuka, E.B. Agbaji, V.O. Ajibola, F.G. Okibe, Treatment of crude oil-contaminated water with chemically modified natural fiber, Appl. Water Sci. 8 (2018) 86.

[7] C. Wong, T. McGowan, S.G. Bajwa, D.S. Bajwa, Impact of fiber treatment on the oil absorption characteristics of plant fibers, Bio. Resources. 11 (2016) 6452–6463.

[8] M. Zamparas, D. Tzivras, V. Dracopoulos, T. Ioannides, Application of sorbents for oil spill cleanup focusing on natural-based modified materials: A review, Molecules. 25 (2020) 4522–4535.

[9] M.A. Mahmoud, Hydrodynamic separator unit for removal and recovery oil from wastewater, J. Pet. Environ. Biotechnology. 7 (2016) 2–8.

[10] X. Yang, M. Guo, Y. Wu, Q. Wu, R. Removal of emulsified oil from water by fruiting bodies of macro-fungus (Auricularia polytricha), PLoS One. 9 (2014) 95162.

[11] A. Abutaleb, N.Zouli, O. Y.Bakather, M. A.Mahmoud. Performance evaluation of Solanum incanum leaves as a biodegradable adsorbent for oil-spill cleanup in seawater, Alex. Eng. J. 233 (2021) 182–189.

[12] D. Sidiras, F. Batzias, I. Konstantinou, M. Tsapatsis, Simulation of autohydrolysis effect on adsorptivity of

wheat straw in the case of oil spill cleaning, Chemical Engineering Research and Design. 92 (2014) 1781–1791.

[13] D. Angelova, I. Uzunov, S. Uzunova, A. Gigova, L. Minchev. Kinetics of oil and oil products adsorption by carbonized rice husks, Chem. Eng. J. 172 (2011) 306–311.

[14] F. Almeida, L. Meili, J. Soletti, K. Esquerre, L. Ribeiro, C. de Farias Silva, Oil produced water treatment using sugarcane solid residue as biosorbent, Revista Mexicana de Ingenier´ıa Qu´ımica. 18 (2019) 27–38.

[15] M.A. Mahmoud, Oil spill cleanup by waste flax fiber: Modification effect, sorption isotherm, kinetics and thermodynamics, Arabian Journal of Chemistry. 13 (2020) 5553–5563

[16] J. Wang, Y. Zheng, and A. Wang, Super hydrophobic kapok fiber oil-absorbent: preparation and high oil absorbency, Chem. Eng. J. 213 (2012) 1–7.

[17] G. Alaa El-Din, A.A. Amer, G. Malsh, M. Hussein, Study on the use of banana peels for oil spill removal, Alexandria Engineering Journal. 57 (2018) 2061–2068.

[18] J. Wang, F. Han, B. Liang, G. Geng, Hydrothermal fabrication of robustly super hydrophobic cotton fibers for efficient separation of oil/water mixtures and oil-in-water emulsions, J. Ind. Eng. Chem. 54 (2017) 174–183.

[19] I.A. El Gheriany, F.A. El Saqa, A.A. Amer, M. Hussein, Oil spill sorption capacity of raw and thermally modified orange peel waste. Alexandria Engineering Journal. 59 (2020) 925–932.

[20] T. A. Saleh. Protocols for synthesis of nanomaterials, polymers, and green materials as adsorbents for water treatment technologies, Environmental Technology & Innovation.24(2021)101821.

[21] A. Q. Al-Gamal, T. A. Saleh, F. Alghunaimi. Nanofiltration Membrane with High Flux and Oil Rejection Using Graphene Oxide/ β-Cyclodextrin for Produced Water Reuse. Materials Today Communications, 31(2017) 103438.

[22] M. Husseien, A.A. Amer, A. El-Maghraby, N.A. Taha, Availability of barley straw application on oil spill clean-up, Int. J. Environ. Sci. Technol. 6 (2009) 123–130.

[23] O.Y. Bakather, N. Zouli, A. Abutaleb, M.A. Mahmoud, A. Daher, M. Hassan, M.A. Eldoma, S.O. Alaswed, Adel A. Fowad, Uranium (VI) ions uptake from liquid wastes by solanum incanum leaves: Biosorption, desorption and recovery, Alexandria Engineering Journal. l59 (2020) 1495–1504.

[24] T. A. Saleh,The influence of treatment temperature on the acidity of MWCNT oxidized by HNO3 or a mixture of HNO3/H2SO4, Applied surface science 257 (17) (2011) 7746-7751.

[25] T. A. Saleh, Simultaneous adsorptive desulfurization of diesel fuel over bimetallic nanoparticles loaded on activated carbon, Journal of cleaner production 172(2018) 2123-2132.

[26] T.R. Annunciado, T.H.D. Sydenstricker, S.C. Amico, Experimental investigation of various vegetable fibers as sorbent materials for oil spills, Mar. Pollut. Bull. 50 (2005) 1340–1346.

[27] A. Abutaleb, A.M. Tayeb, M.A. Mahmoud, A.M. Daher, O.A. Desoukyc, O.Y. Bakather, R. Farouq, Removal and recovery of U (VI) from aqueous effluents by flax fiber: Adsorption, desorption and batch adsorber proposal, Journal of Advanced Research. 22 (2020) 153–162.

[28] J. Huang, Z. Yan, Adsorption mechanism of oil by resilient graphene aerogels from oil-water emulsion, Langmuir: Ee ACS Journal of Surfaces and Colloids. 34 (2018) 1890–1898.

[29] M.A. Mahmoud, Adsorption of U (VI) ions from aqueous solution using silicon dioxide nano powder, Journal of Saudi Chemical Society. 22 (2018) 229–238.

[30] R. Behnood, B. Anvaripour, N. Jaafarzadeh, M. Farasati, Oil spill sorption using raw and acetylated sugarcane bagasse, J. Cent. South Univ. 23 (2016) 1618–1625.

# OXIDATION OF CYCLOHEXANE CATALYZED BY POTASSIUM DICHROMATE IN THE PRESENCE OF OXYGENATED SOLVENT AND HYDROGEN PEROXIDE

## Mohammad Ashraf Ali [1,*]

[1] Department of Chemical Engineering, College of Engineering, Jazan University, Jazan 41542, Saudi Arabia.

## *Corresponding author

## Mohammad Ashraf Ali

## Email address:

maali8000@gmail.com

Oxidation of cyclohexane was catalyzed by potassium dichromate in the presence of hydrogen peroxide as the initiator and acetone as the solvent. The parameters studied were the amount of catalyst, reaction temperature, and reaction time. It was established that a higher amount of catalyst as well as reaction temperature and reaction time increased the conversion of cyclohexane. By optimizing the concentration of the catalyst along with the reaction conditions, the conversion of cyclohexane was achieved efficiently. After three hours of reaction at 150 °C in an autoclave using 150 mg of catalyst, 2 ml cyclohexane, 7 ml acetone, and 2 ml $H_2O_2$, the conversion of cyclohexane achieved was 10.8 wt% and the selectivity of cyclohexanol and cyclohexanone (KA oil) was 100%. Besides, no other compounds were detected in the reaction products. The activation energy of cyclohexane oxidation was calculated to be 18.443 kJ/mol. The experimental data were well fitted to first-order reaction kinetics.

*Keywords:* cyclohexane oxidation; KA oil, cyclohexanol and cyclohexanone, potassium dichromate, hydrogen peroxide, acetone, thermocatalysis

## 1.     INTRODUCTION

The selective oxidation of organic compounds having carbon-hydrogen single bonds (C-H) to produce C-OH and C=O bonds is very difficult, which limits the utilization of these compounds [8]. The selective oxidation of cyclohexane is essential in the commercial production of KA oil (a mixture of cyclohexanol and cyclohexanone). KA oil is the main raw material for the production of nylon-6 and nylon-66 [[7, 10-11]. However, the industrial cyclohexane oxidation process is conducted at high temperature (~425K) and high pressure (~2MPa) but still achieved lower cyclohexane conversion with KA oil selectivity of less than 100% [9]. Therefore, it is necessary to develop efficient inexpensive catalysts and optimize mild reaction conditions to achieve higher catalytic efficiency. Bhuyan et al. [1] synthesized SBA-15/Au nanohybrid material having well-dispersed, spherical, single crystalline Au0 NPs having less than 5

nm size. The SBA-15/Au0 offered 48.7% cyclohexane conversion and higher than 95% cyclohexanone selectivity using TBHP without any solvent. The catalyst was reused four times and showed no significant loss in activity. Yuan et al. [13] synthesized a series of cobalt-loaded catalysts supported on mesoporous graphitic carbon nitride ($Co/g-C_3N_4$) and used for cyclohexane oxidation. The cyclohexane conversion of 23.8% and a selectivity of 95.6% was achieved. Xie et al. [12] synthesized $Cu_2O/BGC$ using copper nitrate and carbon derived from Bougainvillea glabra (BGC) plant which showed cyclohexane conversion of 77.1% with cyclohexanone selectivity of 68.5% using TBHP under solvent-free condition. The catalyst was reused five times without any significant loss in activity. Xiang et al. [10] examined the photocatalytic performance of $BiVO_4$ and $Cu_3V_2O_8$ under visible-light irradiation. Results showed that $BiVO_4$ exhibited 95% KA oil selectivity with higher

chemoselectivity (cyclohexanone/cyclohexanol molar ratio = 3.0) than $Cu_3V_2O_8$. Zhang et al. [14] prepared Z-scheme composite catalysts using $WO_3$ nanosheets and nanocarbon dots (NCD) for cyclohexane oxidation. The $WO_3$-NCDs exhibited better catalytic activity in photocatalysis, thermocatalysis, and photothermal catalysis and showed 7.88% photothermal oxidation of cyclohexane which was 1.5 times higher than pure $WO_3$ nanosheets. Wan et al. [9] carried out photocatalytic oxidation of cyclohexane using $VOCl_2$ in acetonitrile solution under Xe lamp irradiation in $O_2$ atmosphere. The results showed cyclohexane conversion of 17.8% with 99% selectivity for KA oil after light irradiation for 4 h. The use of HCl enhanced the photocatalytic oxidation of cyclohexane conversion to 23.3%. Xiao et al [11] synthesized silver NPs coupled with $WO_3$ nanocrystals (Ag NPs-$WO_3$ NCs) and used for selective photoxidation of cyclohexane. The photocatalytic activity of $WO_3$ nanosheet-Ag NPs composite ($WO_3$ NSs-Ag NPs) was 1.3 times higher compared to $WO_3$ nanocube-Ag NPs composites ($WO_3$ NCs-Ag NPs). The highest cyclohexane conversion to KA oil achieved was 40.2% with 97.0% selectivity under solar light irradiation at room temperature. The $WO_3$ NSs-Ag NPs shows photocatalytic stability without any loss of catalytic activity even after ten cycles. Shiraishi et al [7] synthesized $TiO_2$ with reduced graphene oxide (rGO), and catalyzed cyclohexane to cyclohexanone with enhanced activity and selectivity under UV light ($\lambda > 300$ nm). The $TiO_2$/rGO catalyst showed higher cyclohexanone selectivity (>80%) compared to $TiO_2$ (~60%). Zhang et al. [15] synthesized triazine-based carbon nitride and used it as an efficient photocatalyst for cyclohexane selective oxidation (5.81% conversion and over 99.9% cyclohexanone selectivity) using air and water only. Ide et al. [2] reported the synthesis of mesoporous silica containing isolated tetrahedrally coordinated Ti and Fe oxide NPs immobilized on the surface of SBA-15 with Ti(IV) acetylacetonate and Fe(III) acetylacetonate successively. These catalysts showed high yield and almost 100% selectivity for KA oil with molecular $O_2$ under solar light. Tong et al. [8] synthesized a silica-supported magnetic cobalt ferrite complex, $CoFe_2O_4$/$SiO_2$, with different loadings (5, 10, 20, and 50%) and used for cyclohexane oxidation. The 5%$CoFe_2O_4$/$SiO_2$ catalysts showed 95.4% selectivity for KA oil at 1.6 MPa oxygen pressure and 145 ºC after 6 h of reaction. All catalysts showed good recyclability with no significant loss in activity after six

consecutive runs. R. Liu et al. [4] reported the synthesis of composites using metal NPs and carbon quantum dots (CQDs), Au NPs/CQDs composite photocatalyst yielded 63.8% cyclohexane conversion and 99.9% KA oil selectivity using $H_2O_2$ under visible light at room temperature. J. Liu et al. [3] demonstrated the synthesis of composites made from Au NPs and carbon nitride ($C_3N_4$) and achieved 10.5% cyclohexane conversion and 100% selectivity to cyclohexanone under visible light without any oxidant or initiator.

This research utilized potassium dichromate to achieve cyclohexane conversion to cyclohexanone and cyclohexanol under moderate temperature and hydrothermal pressure.
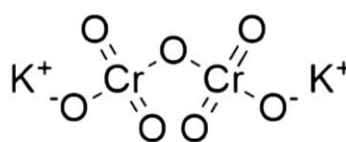


Potassium dichromate
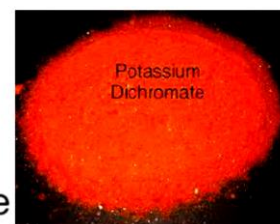
## 2.  EXPERIMENTAL

### 2.1. CHEMICALS AND MATERIALS

The chemicals utilized in this study were cyclohexane (purity 99%), hydrogen peroxide (purity 30%), Catalyst: potassium dichromate (purity 99%), acetone (purity 99%). All chemicals were purchased from Sigma Aldrich and utilized without further treatment

### 2.2. THERMOCATALYTIC REACTION PROCEDURE

The reaction procedure adopted was as follows: In a clean steel autoclave having Teflon container with Teflon lid, cyclohexane was added along with acetone and $H_2O_2$. The catalyst was then added and the contents were thoroughly mixed. The autoclave was then sealed and heated in a furnace for a specified time and temperature. The autoclave was heated at the rate of 5 °C per min. The time of reaction was calculated after the autoclave reached the required temperature. At the end of the reaction, the autoclave was allowed to cool, then removed from the furnace and cooled in an ice bath. Once the autoclave attained sub-room temperature, it was opened and the contents were poured in a glass tube. The reaction products were then separated from other components and sealed in a vial for analysis. The products were analyzed by GC-MS to determine the conversion of cyclohexane and the amount of cyclohexanol and cyclohexanone produced. The effect of reaction time (1, 2, 3 hours),

reaction temperature (100, 125, 150 ℃), and amount of catalyst (100, 150, and 200 mg), were studied to establish their effect on the cyclohexane conversion and product selectivity. The amounts of cyclohexane, acetone, and $H_2O_2$ were optimized to 2, 7, and 2 ml, respectively, in several experiments.

### 2.3. REACTION PRODUCT ANALYSIS BY GCMS

The gas chromatography mass spectrometry (GC-MS) analysis was performed using Shimadzu GC-MS system (model QP2010 Ultra). The details of GC-MS analysis have been reported earlier [5]. Briefly, the reaction products were separated on a capillary column using helium carrier gas. The operating conditions were as follows: sample volume injected 1.0 µL, injection port temperature 290 °C, oven 30 °C to 300 °C, MS, ion source 230 °C and Interface at 280 °C. Total ion chromatogram was generated for the m/z range 30-200. The component peaks were identified by comparing their mass spectra with the spectra in the GC-MS system database and quantified based on area percent. The GC-MS spectrum obtained for a product sample is shown in **Figure 1**.
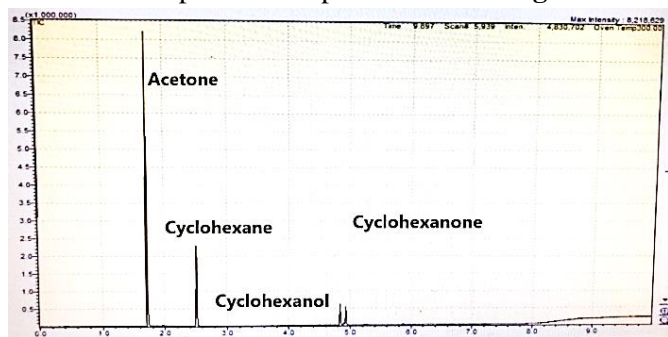


**Fig. 1.** Chromatogram of a reaction product showing the peak position of cyclohexane, acetone, and the reaction products, cyclohexanone and cyclohexanol

## 3.     RESULTS AND DISCUSSION

### 3.1   CYCLOHEXANE CONVERSION

The cyclohexane conversion results are shown in **Figure 2**. The cyclohexane conversion showed an increasing trend with increase in the amount of catalyst from 100 to 200 mg at 125 ℃. **(Figure 2a)**. The increase in reaction temperature from 100 to 150 ℃ has also increased the trend for cyclohexane conversion as shown in **Figure 2b**. The detailed results are given in Table 1.
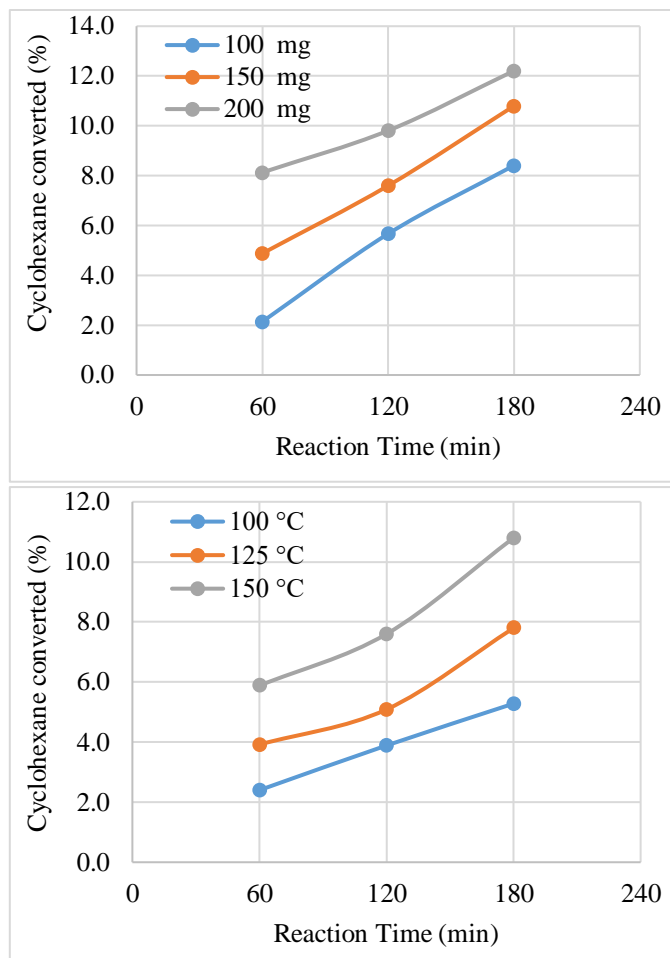


**Fig. 2. a.** Plot of cyclohexane converted as a function of reaction time at variable amount of catalyst. The reaction conditions were as follows: Catalyst amount 100-200 mg, reaction temperature 150 ℃, cyclohexane 2 ml, acetone 7 ml, and 2 ml $H_2O_2$. **b.** Plot of cyclohexane converted as a function of reaction time at variable reaction temperatures. The reaction conditions were as follows: Reaction temperature 100-150 ℃, amount of catalyst 150 mg, cyclohexane, cyclohexane 2 ml, acetone 7 ml, and 2 ml $H_2O_2$.

**Table 1.** *Results of Cyclohexane oxidation to produce cyclohexanone and cyclohexanol. The reaction conditions were as follows: amount of catalyst 150 mg, cyclohexane 2 ml, acetone 7 ml, and 2 ml $H_2O_2$.*

| Wt% cyclohexane conversion | | | |
|---|---|---|---|
| | **Reaction Temperature** | | |
| **Time, minutes** | **100 °C** | **125 °C** | **150 °C** |
| **60** | 2.40 | 3.92 | 5.88 |
| **120** | 3.89 | 5.09 | 7.60 |
| **180** | 5.28 | 7.80 | 10.8 |
| **gm of cyclohexane converted** | | | |
| **Time, minutes** | **100 °C** | **125 °C** | **150 °C** |
| **60** | 0.05 | 0.08 | 0.12 |
| **120** | 0.08 | 0.10 | 0.15 |

| 180 | 0.11 | 0.16 | 0.22 |

| mg of cyclohexane converted | | | |
|---|---|---|---|
| Time, minutes | 100 °C | 125 °C | 150 °C |
| 60 | 48.0 | 78.4 | 117.6 |
| 120 | 77.8 | 101.8 | 152.0 |
| 180 | 105.6 | 156.0 | 216.0 |

| mg of cyclohexane converted/mg of catalyst | | | |
|---|---|---|---|
| Time, minutes | 100 °C | 125 °C | 150 °C |
| 60 | 0.32 | 0.52 | 0.78 |
| 120 | 0.52 | 0.68 | 1.01 |
| 180 | 0.70 | 1.04 | 1.44 |

### 3.2. KINETIC MODELS

The data used for the kinetic study are shown in Table 2 and the plots are given in Figure 3 and Figure 4. It was clearly observed that the amount of cyclohexane consumed with increasing the reaction time used in the reaction mixture.

*Percent Conversion of Cyclohexane = 100 x [($C_0$ – $C_t$) / $C_0$]*

The reaction rate was deduced from the plot of the concentration of cyclohexane as a function of reaction time. Reaction Rate = k (Concentration of cyclohexane) For all initial concentrations of cyclohexane, the conversion follows the first-order reaction. Therefore, the time-dependent plot was fitted with either a single exponential function, $C_t = C_0 e^{-kt}$ or a logarithmic function, *Ln $C_t$ = -kt + Ln $C_0$*. Finally, the following equation was used to plot the Ln $C_t$/Co against t and get the rate constant for the reaction.

*Ln $C_t$/Co = -kt*

Where $C_0$ and $C_t$ are the initial concentration of cyclohexane and the concentration of cyclohexane after reaction t, respectively, and k is the rate constant of the reaction. Table 3 shows the rate constant (k) and the correlation coefficient ($R^2$) values for the conversion of cyclohexane into KA oil.

**Table 2.** *Data used for the kinetic study. The amount of catalyst was 150 mg.*

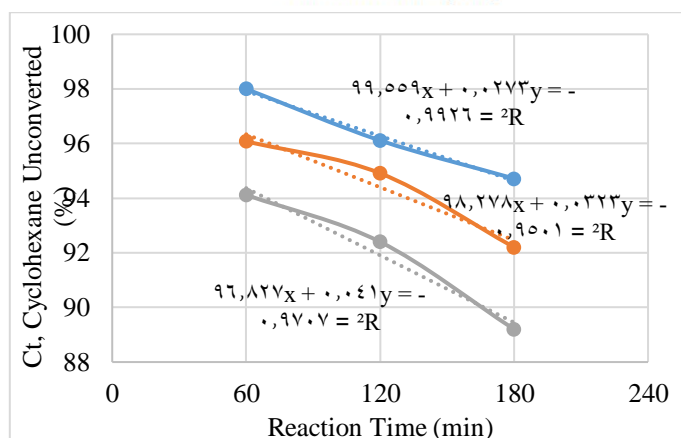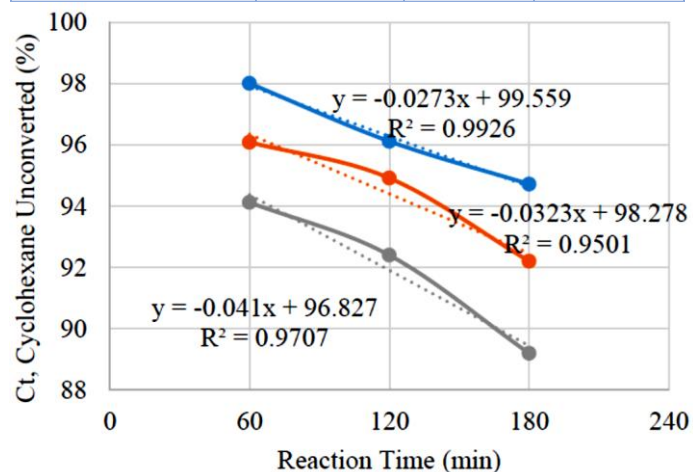| Wt% cyclohexane converted | | | |
|---|---|---|---|
| Reaction Time, min | Reaction Temperature | | |
| | 100 °C | 125 °C | 150 °C |
| 60 | 2.40 | 3.92 | 5.88 |
| 120 | 3.89 | 5.09 | 7.60 |
| 180 | 5.28 | 7.80 | 10.80 |
| | Ct Wt% cyclohexane unconverted | | |
| | 100 °C | 125 °C | 150 °C |
| 60 | 97.60 | 96.08 | 94.12 |
| 120 | 96.11 | 94.91 | 92.40 |
| 180 | 94.72 | 92.20 | 89.20 |
| | Ln Ct Wt% cyclohexane unconverted | | |
| | 100 °C | 125 °C | 150 °C |
| 60 | -4.58088 | -4.56520 | -4.54457 |
| 120 | -4.56553 | -4.55295 | -4.52613 |
| 180 | -4.55091 | -4.52400 | -4.49088 |





**Fig. 3.** Plot of unreacted cyclohexane (Ct) vs reaction time (min). The reaction conditions were as follows: Reaction temperature 100-150 °C, amount of catalyst 150 mg, cyclohexane 2 ml, acetone 7 ml, and 2 ml $H_2O_2$.



**Fig. 4.** Plot of Ln Ct vs reaction time (min). The reaction conditions were as follows: Reaction temperature 100-150 °C,

amount of catalyst 150 mg, cyclohexane 2 ml, acetone 7 ml, and 2 ml $H_2O_2$.
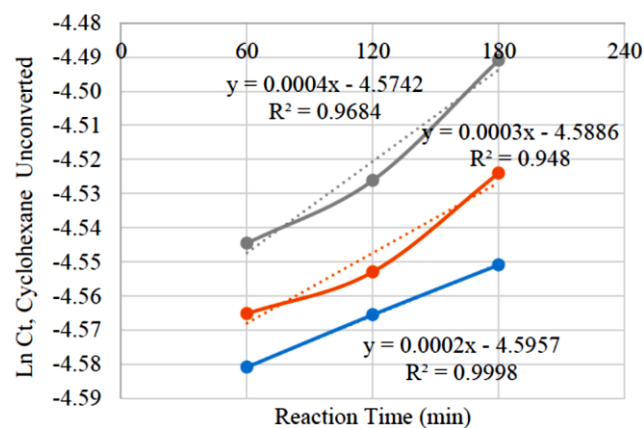
**Table 3.** *Rate constant (k) and correlation coefficient ($R^2$) values for the conversion of cyclohexane into KA oil.*

| Time, min | Reaction Temperature, °C (K) | Ln Ct vs Time first order reaction kinetics ($h^{-1}$) | | | | |
|---|---|---|---|---|---|---|
| | | 1/T (K) | Slope (k) ($min^{-1}$) | Slope (k) ($h^{-1}$) | $R^2$ | Ln k |
| 60 | 100 (373) | 0.00268 | 0.0002 | 0.0000033 | 0.9998 | -12.6115 |
| 120 | 125 (398) | 0.00251 | 0.0003 | 0.0000050 | 0.9480 | -12.2061 |
| 180 | 150 (423) | 0.00236 | 0.0004 | 0.0000067 | 0.9684 | -11.9184 |

### *3.3  ACTIVATION ENERGY CALCULATION*

The activation energy of the cyclohexane oxidation was calculated by a graphical method. The natural log of the rate constant (Ln k) was plotted as a function of the reciprocal of absolute temperature (1/T) and the value of slope was obtained (**Figure 5**). The value of the slope was multiplied with the value of the gas constant (R) to obtain the activation energy.
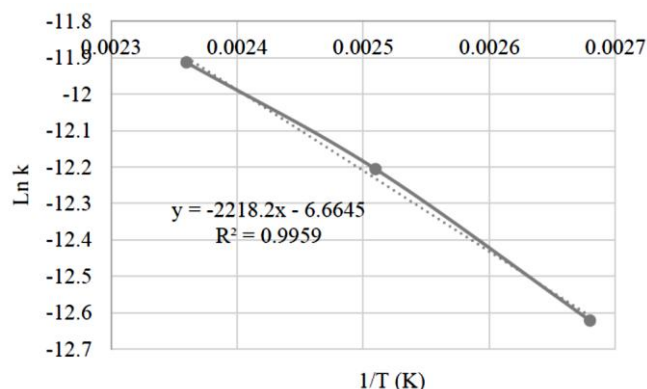


**Fig. 5.** Plot of the natural log of the rate constant (Ln k) as a function of the reciprocal of absolute temperature (1/T).

Slope = 2218.2 = Ea/R, R = 8.314 $J.mol^{-1}.K^{-1}$. Therefore, the activation energy (Ea) was calculated as follows: Ea = Slope x R = 2218.2 x 8.3144598 = 18443 J/mol = 18.443 kJ/mol. Thus, the activation energy value calculated was 18.443 kJ/mol, which is much lower than the reported literature values. An activation energy of 71.2 kJ/mol has been reported by M. Sadiq et al. [6] for cyclohexane oxidation to produce cyclohexanol and cyclohexanone at 75 °C using activated charcoal. Other conditions were as follows: reaction time 14 hours, oxygen flow 40 mL/min ($pO_2$ 760 torr), catalyst amount 0.4 g, and cyclohexane amount 115.56 mmol

## 4.     CONCLUSIONS

The Oxidation of cyclohexane was accomplished efficiently by potassium dichromate in the presence of hydrogen peroxide and acetone. The optimal conditions for the experiment were achieved after several trials and it was found that increasing the amount of catalyst as well as temperature and reaction time increased the conversion of cyclohexane. After three hours of reaction in an autoclave, the conversion of cyclohexane achieved was 10.8 wt% and the product (cyclohexanol and cyclohexanone) selectivity was 100%. Besides, no other compounds were detected in the reaction products. The activation energy of cyclohexane oxidation to produce cyclohexanol and cyclohexanone was calculated to be 18.443 kJ/mol. The experimental data was well fitted to a first-order reaction kinetics.

## 5.     DATA AVAILABILITY STATEMENT:

## 6.     FUNDING STATEMENT:

## 7.     CONFLICTS OF INTEREST:

The authors declare no conflict of interest.

## 8.     ACKNOWLEDGMENT:

## 9.     REFERENCES

[1]   Bhuyan, D.; S. J. Kalita and L. Saikia, Mesoporous SBA-15 supported gold nanoparticles for solvent-free oxidation of cyclohexane: superior catalytic activity with higher cyclohexanone selectivity, Phys. Chem. Chem. Phys., 2022, 24, 29781. https://doi.10.1039/d2cp04198g

[2]   Ide, Y.; M. Iwata, Y. Yagenji, N. Tsunoji, M. Sohmiya, K. Komaguchi, T. Sanoc, Y. Sugahara, Fe oxide nanoparticles/Ti-modified mesoporous silica as a photocatalyst for efficient and selective cyclohexane conversion with O2 and solar light, J. Mater. Chem. A Mater. Energy Sustain. 4 (2016) 15829–15835, https://doi.org/10. 1039/c6ta04222h.

[3]   Liu, J.; Y. Yang, N. Liu, Y. Liu, H. Huang, Z. Kang, Total photocatalysisconversion from cyclohexane to cyclohexanone by $C_3N_4$/Au nanocomposites, Green

Chem. 16 (2014) 4559–4565. https://doi.org/10.1039/c4gc01126k.

[4] Liu, R.; H. Huang, H. Li, Y. Liu, J. Zhong, Y. Li, S. Zhang, Z. Kang, Metal nanoparticle/carbon quantum dot composite as a photocatalyst for high-Efficiency cyclohexane oxidation, AcsCatal. 4 (2014) 328–336. https://doi.org/10.1021/ cs400913h.

[5] Ali, M.A. M.D.Y Oteef, A. Yusuf, A. Abutaleb, S. Matar, M. ELHalwany (2022). Efficient liquefaction of lignin in methanol using $ZrO_2$ electrospun nanofibrous catalyst, *Jazan University Journal*, 10(1), 33-47.

[6] Sadiq, M.; Mashooq Khan, Muhammad Numan, Razia Aman, Saddam Hussain, M. Sohail Ahmad, Saima Sadiq, Muhammad Abid Zia, Haroon Ur Rashid, and Rahmat Ali, Tuning of Activated Carbon for Solvent-Free Oxidation of Cyclohexane, Hindawi Journal of Chemistry Volume 2017, Article ID 5732761, 8 pages https://doi.org/10.1155/2017/5732761.

[7] Shiraishi, Y.; S. Shiota, H. Hirakawa, S. Tanaka, S. Ichikawa, T. Hirai, Titanium Dioxide/Reduced graphene oxide hybrid photocatalysts for efficient and selective partial oxidation of cyclohexane, ACS Catal. 7 (2017) 293–300. https://doi.org/10.1021/acscatal.6b02611

[8] Tong, J.; L. Bo, X. Cai, H. Wang, Q. Zhang, L. Su, Aerobic oxidation of cyclohexane effectively catalyzed by simply synthesized silica-supported cobalt ferrite magnetic nanocrystal, Ind. Eng. Chem. Res. 53 (2014) 10294–10300, https://doi.org/10.1021/ie5008213.

[9] Wan, Y.; Q. Guo, K. Wang, X. Wang, Efficient and selective photocatalytic oxidation of cyclohexane using O2 as oxidant in $VOC_{l2}$ solution and mechanism insight, Chem. Eng. Sci. 203 (2019) 163–172. https://doi.org/10.1016/j.ces.2019.03.079

[10] Xiang, L.; Jingjing Fan, Wenzhou Zhong, Liqiu Mao, Kuiyi You, Dulin Yin, Heteroatom-induced band-reconstruction of metal vanadates for photocatalytic cyclohexane oxidation towards KA-oil selectivity, Applied Catalysis A: General, 575, 2019, 120-131. https://doi.org/10.1016/j.apcata.2019.02.015.

[11] Xiao, Y.; J. Liu, J. Mai, C. Pan, X. Cai, Y. Fang, High-performance silver nanoparticles coupled with monolayer hydrated tungsten oxide nanosheets: the structural effects in photocatalytic oxidation of cyclohexane, J. Colloid Interf. Sci. 516 (2018) 172–181. https://doi.org/10.1016/j.jcis.2018.01.057

[12] Xie, C.; Qi Xiong, Liang Jiang, Yuanfeng Wang, Qinyuan Tang, Jiao He, Jiaqiang Wang, Carbon supported copper catalyst prepared in situ by one-pot pyrolysis of Bougainvillea glabra: An efficient and stable catalyst for selective oxidation of cyclohexane, Applied Surface Science, 576, Part B, 2022, 151833. https://doi.org/10.1016/j.apsusc.2021.151833.

[13] Yuan, E.; Zhou, M., Shi, G. et al. Ultralow-loading single-atom cobalt on graphitic carbon nitrogen with robust Co-N pairs for aerobic cyclohexane oxidation. Nano Res. 15, 8791–8803 (2022). https://doi.org/10.1007/s12274-022-4556-3.

[14] Zhang, J.; Jincheng Liu , Xiaoyu Wang, Jijin Mai, Wei Zhao, Zhongxiang Ding, Yanxiong Fang, Construction of Z-scheme tungsten trioxide nanosheets-nitrogen-doped carbon dots composites for the enhanced photothermal synergistic catalytic oxidation of cyclohexane, Applied Catalysis B: Environmental Volume 259, 2019, 118063. https://doi.org/10.1016/j.apcatb.2019.118063

[15] Zhang, Y.; L. Hu, C. Zhu, J. Liu, H. Huang, Y. Liu, Z. Kang, Air activation by a metalfree photocatalyst for "totally-green" hydrocarbon selective oxidation, Catal.Sci. Technol. 6 (2016) 7252–7258, https://doi.org/10.1039/c6cy01066k

# REFINED HIGHER-ORDER SHEAR DEFORMATION THEORY FOR VIBRATION ANALYSIS OF FUNCTIONALLY GRADED SANDWICH BEAM ON PASTERNAK FOUNDATIONS

**Ali Alnujaie**

Mechanical Engineering Department, Faculty of Engineering, Jazan University, P. O. Box 45142, Jazan, Kingdom of Saudi Arabia

**\*Corresponding author**

**Ali Alnujaie**

**Email address:**

aalnajei@jazanu.edu.sa

The objective of this research is to introduce a new higher-order shear deformation theory that utilizes only three unknown variables. This theory is then implemented in the analysis of the vibration characteristics of sandwich beams. The study focuses on hard-core sandwich beams consisting of a ceramic gradient core and two functionally graded material face-sheets, placed on a two-parameter foundation modeled by Pasternak's type foundations. The equations of motion are established using Hamilton's principle, and the Navier solution method is employed for obtaining numerical results. To verify the accuracy of the proposed theory, a comparison study is conducted. Additionally, the study investigates the effects of various factors, including the length-to-thickness ratio, material gradient index, the ratio of the layers' thickness, and elastic foundation parameters.

*Keywords:* *beams; vibration; functionally graded; Pasternak's foundations; hard-core n*

## 1. INTRODUCTION

The development of advanced materials for engineering and industrial purposes is a critical task for researchers. Functionally graded materials (FGMs) are among the most widely used advanced materials [1–5], and thus, researchers worldwide have studied the static and dynamic behaviors of FG structures [6,7], particularly FG beams, which have various applications in automobile engineering, civil engineering, mechatronics, and other fields. In the past, the Euler-Bernoulli beam theory was developed and utilized for the analysis of thin beam structures. Researchers such as Wang et al. [8], Nguyen [9], Lee et al. [10], and Shahba et al. [11] applied this

theory to the analysis of free vibration, large displacement behavior of tapered cantilever FG beams, and free vibration and stability of FG beams, respectively, using differential transform method (DTM). However, this theory is not compatible with the analysis of thick beams due to its neglect of transverse shear stress in the height direction. To overcome this limitation, the Timoshenko beam theory and first-order shear deformation beam theory (FSDT) were developed for the analysis of moderate structures [12,13]. Researchers such as Kien et al. [14], Zang et al. [15], and Vinh [16] used FSDT to analyze the static and vibration of axially load FG beams, the mechanical behaviors of FG graphene oxide-reinforced composite beams, and the functionally

graded sandwich (FGS) beams, respectively, using a novel mixed beam element based on FSDT. For thick beam structures, higher-order shear and normal deformation theories (HSDTs) and quasi-3D theories have been established for the investigation of isotropic and composite beams as well as FG beams. In addition to static analysis, free vibration analysis is also a significant problem in engineering fields. Nguyen et al. [17] used an HSDT for vibration and buckling analysis of sandwich beams, while Kadoli et al. [18] analyzed the static bending of FG beams using a new HSDT. In a study by Luat and colleagues [18], the vibration performance of nano-scale FGS beams was analyzed. The authors introduced a novel sandwich beam structure consisting of a homogeneous core and distinct FG face sheets. Thai and colleagues [19] employed different HSDTs to examine static and dynamic responses of FG beams and obtained new findings. Uddin and co-workers [20] investigated the large deformation behaviors of composite beams with partial shear interaction by employing HSDT. He and colleagues [21,22] developed an analytical solution for buckling, vibration, and dynamic analysis of composite beams using HSDT. Nguyen and colleagues [23] proposed a new HSDT that incorporated a novel shear distribution function to analyze the bending, vibration, and buckling behaviors of FG sandwich beams. Askari and co-authors [24] investigated the vibration of piezoelectric FG porous beams with coupled transverse and shear effects using HSDT. Riadh and his team [25] developed a new HSDT and quasi-3D theories that utilized a hyperbolic distribution function to analyze the mechanical properties of FG beams. Li et al. [26] introduced a mixed beam element that utilizes HSDT to enhance the convergence rate of finite element analysis for FGS beams. Frikha et al. [27] also proposed a C0 mixed beam element based on HSDT for static bending analysis of FG beams. This approach considers the nonlinear distribution of the shear stress through the thickness direction and incorporates four unknown variables in the displacement field. Furthermore, Li et al. [28] developed a new HSDT with modified shape functions to describe the transverse shear stress, which was utilized to investigate both static and dynamic behaviors of FG beams. Simsek [29] investigated the vibration behavior of FG beams using various HSDTs introduced by different authors to determine the most effective theory. Karamanli et al. [30] proposed a new microbeam theory-based quasi-3D theory to analyze the

behavior of micro-FG beams. Osofero et al. [31] used several quasi-3D theories to examine the vibration and buckling behaviors of beams. Vo et al. [32] developed a novel quasi-3D theory with a sinusoidal function of shear stress to analyze the vibration and buckling of FG sandwich beams. Yu et al. [33] presented a new size-dependent quasi-3D theory for isogeometric analysis of FG microbeams. Additionally, Fang et al. [34] employed isogeometric analysis in conjunction with quasi-3D theory to analyze porous FG beams.

This research introduces a new HSDT for analyzing the vibration characteristics of sandwich beams. The proposed HSDT comprises only three unknown variables and ensures that the free surfaces of the beams satisfy the free condition of shear stress. Furthermore, the HSDT does not require a correction factor and is therefore suitable for analyzing both thin and thick beams. The accuracy of the proposed theory is validated through a comparison study. Additionally, a parameter study is conducted to investigate the effects of various factors on the vibration behavior of the beams. The study also presents new numerical results, which can serve as benchmark results for future work.

## 2. THEORETICAL FORMULATION

### 2.1. GEOMETRICAL AND MATERIAL MODELLING

For numerica1 analysis, an FGS beams as shown in Fig. 1 is studied. The foundations are modelled by Pasternak elastic foundations. The length of beam is $a$ , the heigh is $h_t$ in total and $h_c$ for two skin layers. The coordinates of the layer are $z_0$, $z_1$, $z_2$ and $z_3$ as presented in Fig. 1.
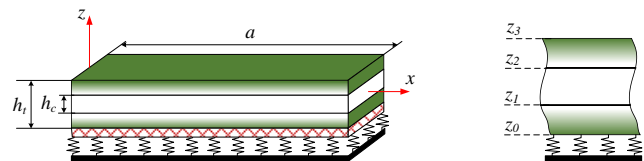


**Fig. 1.** Geometrical modeling of FGS beams

The following formulation is used to evaluate the volume fraction of the ceramic component

$$
\begin{cases}
V_c^{bottom} = \left(\dfrac{z-z_0}{z_1-z_0}\right)^k & z_0 \le z \le z_1 \\[2mm]
V_c^{core} = 1 & z_1 < z < z_2 \\[2mm]
V_c^{top} = \left(\dfrac{z-z_3}{z_2-z_3}\right)^k & z_2 \le z \le z_3
\end{cases}
\tag{1}
$$

The material properties of the FGS beams are calculated as follows (Nguyen et a1. [23])

$$
\begin{aligned}
E(z) &= E_c V_c + E_m(1-V_c) \\
\rho(z) &= \rho_c V_c + \rho_m(1-V_c)
\end{aligned}
\tag{2}
$$

where $E$, $\rho$ are, respectively, Young's moduli, the mass densities and script $c$, $m$ are used to denote for ceramic and metal. Due to the fact that the effects of the Poisson's ratio on the mechanical behaviors of the structures is small, so, the Poisson's ratio is assumed to be constant in this study.

### 2.2. NEW REFINED BEAM THEORY

In the new higher-order shear deformation theory, the FGS beams' displacement field can be expressed in the following manner

$$
u(x,z) = u(x) - z\frac{\partial w_b}{\partial x} - \Phi(z)\frac{\partial w_s}{\partial x}
\tag{3}
$$

$$
w(x,z) = w_b(x) + w_s(x)
$$

The function $\Phi(z)$ in the equation fulfills the free surface conditions for transverse shear stress in FGS beams. Additionally, a new function $\Phi(z)$ can be defined in the following manner

$$
\Phi(z) = 5z - 5h\tan^{-1}\left(\frac{z}{h}\right)
\tag{4}
$$

The strain fields can be expressed as follows

$$
\varepsilon_x = \frac{\partial u}{\partial x} - z\frac{\partial^2 w_b}{\partial x^2} - \Phi\frac{\partial^2 w_s}{\partial x^2}
\tag{5}
$$

$$
\gamma_{xz} = (1-\Phi')\frac{\partial w_s}{\partial x}
$$

The stresses and strains of the FGS beams are related by the following equations

$$
\begin{Bmatrix} \sigma_x \\ \tau_{xz} \end{Bmatrix} = \begin{bmatrix} E(z) & 0 \\ 0 & G(z) \end{bmatrix} \begin{Bmatrix} \varepsilon_x \\ \gamma_{xz} \end{Bmatrix}
\tag{6}
$$

where $G(z) = E(z)/(2(1+v))$.

In order to derive the equations of motion for FGS beams, Hamilton's principle is utilized as shown in the following equation

$$
0 = \int_0^T \left(\delta\Pi_f + \delta\Pi - \delta T\right)dt
\tag{7}
$$

where $\delta\Pi$ is the variation of the strain energy, $\delta\Pi_f$ and $\delta T$ is the variation of the kinematic energy. The variation of the strain energy is obtained as the following expression

$$
\delta\Pi = \int_0^L \int_A \left(\sigma_x \delta\varepsilon_x + \sigma_{xz}\delta\varepsilon_{xz}\right)dAdx
\tag{8}
$$

Integrating through the thickness of the FGS beams, one gets

$$
\delta\Pi = \int_0^L \left(N\frac{\partial\delta u}{\partial x} - M\frac{\partial^2\delta w_b}{\partial x^2} - P\frac{\partial^2\delta w_s}{\partial x^2} + Q\frac{\partial\delta w_s}{\partial x}\right)dx
\tag{9}
$$

where $N$, $M$, $P$ and $Q$ are the stress resultants which are

$$
(N,M,P) = \int_A (1, z, \Phi)\sigma_x dA
$$

$$
Q = \int_A \sigma_{xz}(1-\Phi')dA
\tag{10}
$$

Inserting Eq. (6) into Eq. (10), one gets

$$
\begin{Bmatrix} N \\ M \\ P \end{Bmatrix} = \begin{bmatrix} A & B & X \\ B & D & F \\ X & F & H \end{bmatrix} \begin{Bmatrix} \dfrac{\partial u}{\partial x} \\[2mm] -\dfrac{\partial^2 w_b}{\partial x^2} \\[2mm] -\dfrac{\partial^2 w_s}{\partial x^2} \end{Bmatrix}
\tag{11}
$$

$$
Q = S\frac{\partial w_s}{\partial x}
\tag{12}
$$

where

$$
(A, B, X, D, F, H) = \int_A E(z)\left(1, z, \Phi, z^2, z\Phi, \Phi^2\right)dA
\tag{13}
$$

$$
S = \int_A G(z)(1-\Phi')dA
\tag{14}
$$

The energy stored in elastic foundations can be expressed as

$$
\delta\Pi_f = \int_0^L \left(k_w(w_b+w_s)\delta(w_b+w_s) + k_s\frac{\partial(w_b+w_s)}{\partial x}\frac{\partial\delta(w_b+w_s)}{\partial x}\right)dx
\tag{15}
$$

The kinematic energy of the FGS beams is calculated as

$$\delta T = \int_0^L \int_A \left( \dot{u}\delta\dot{u} + \dot{w}\delta\dot{w} \right) \rho dAdx \tag{16}$$

$$\delta T = \int_0^L \int_A \left( \dot{u} - z\frac{\partial \dot{w}_b}{\partial x} - \Phi\frac{\partial \dot{w}_s}{\partial x} \right) \rho(z) \left( \delta\dot{u} - z\frac{\partial \delta\dot{w}_b}{\partial x} - \Phi\frac{\partial \delta\dot{w}_s}{\partial x} \right)$$
$$+ \left( \dot{w}_b + \dot{w}_s \right)\rho\left( \delta\dot{w}_b + \delta\dot{w}_s \right) dAdx \tag{17}$$

After integrating through the thickness of the FGS beams, one gets

$$\delta T = \int_0^L \left[ I_0\left( \dot{u}\delta\dot{u} + (\dot{w}_b + \dot{w}_s)(\delta\dot{w}_b + \delta\dot{w}_s) \right) + I_1\left( \dot{u}\frac{\partial \delta\dot{w}_b}{\partial x} + \frac{\partial \dot{w}_b}{\partial x}\delta\dot{u} \right) + I_2\left( \dot{u}\frac{\partial \delta\dot{w}_s}{\partial x} + \frac{\partial \dot{w}_s}{\partial x}\delta\dot{u} \right) + \right.$$
$$\left. + I_3\left( \frac{\partial \dot{w}_b}{\partial x}\frac{\partial \delta\dot{w}_b}{\partial x} \right) + I_4\left( \frac{\partial \dot{w}_b}{\partial x}\frac{\partial \delta\dot{w}_s}{\partial x} + \frac{\partial \dot{w}_s}{\partial x}\frac{\partial \delta\dot{w}_b}{\partial x} \right) + I_5\left( \frac{\partial \dot{w}_s}{\partial x}\frac{\partial \delta\dot{w}_s}{\partial x} \right) \right] dx \tag{18}$$

where

$$(I_0, I_1, I_2, I_3, I_4, I_5) = \int_A \rho(z)\left( 1, -z, -\Phi, z^2, z\Phi, \Phi^2 \right) dA \tag{19}$$

Substituting Eq. (9), (15) and Eq. (18) into Eq. (7) and using partially integral, one gets

$$\delta u : -\frac{\partial N}{\partial x} = -I_0\ddot{u} - I_1\frac{\partial \ddot{w}_b}{\partial x} - I_2\frac{\partial \ddot{w}_s}{\partial x},$$

$$\delta w_b : -\frac{\partial^2 M}{\partial x^2} + k_w\left( w_b + w_s \right) - k_s\left( \frac{\partial^2 w_b}{\partial x^2} + \frac{\partial^2 w_s}{\partial x^2} \right)$$
$$= -I_0(\ddot{w}_b + \ddot{w}_s) + I_1\frac{\partial \ddot{u}}{\partial x} + I_3\frac{\partial^2 \ddot{w}_b}{\partial x^2} + I_4\frac{\partial^2 \ddot{w}_s}{\partial x^2},$$

$$\delta w_s : -\frac{\partial^2 P}{\partial x^2} - \frac{\partial Q}{\partial x} + k_w\left( w_b + w_s \right) - k_s\left( \frac{\partial^2 w_b}{\partial x^2} + \frac{\partial^2 w_s}{\partial x^2} \right)$$
$$= -I_0\left( \ddot{w}_b + \ddot{w}_s \right) + I_2\frac{\partial \ddot{u}}{\partial x} + I_4\frac{\partial^2 \ddot{w}_b}{\partial x^2} + I_5\frac{\partial^2 \ddot{w}_s}{\partial x^2}. \tag{20}$$

By substituting Eq. (11) and (12) into Eq. (20), the following equations of motion of the FGS beams are achieved as the following formulae

$$\delta u : A\frac{\partial^2 u}{\partial x^2} - B\frac{\partial^3 w_b}{\partial x^3} - X\frac{\partial^3 w_s}{\partial x^3} = I_0\ddot{u} + I_1\frac{\partial \ddot{w}_b}{\partial x} + I_2\frac{\partial \ddot{w}_s}{\partial x},$$

$$\delta w_b : B\frac{\partial^3 u}{\partial x^3} - D\frac{\partial^4 w_b}{\partial x^4} - F\frac{\partial^4 w_s}{\partial x^4} - k_w\left( w_b + w_s \right) + k_s\left( \frac{\partial^2 w_b}{\partial x^2} + \frac{\partial^2 w_s}{\partial x^2} \right)$$
$$= I_0(\ddot{w}_b + \ddot{w}_s) - I_1\frac{\partial \ddot{u}}{\partial x} - I_3\frac{\partial^2 \ddot{w}_b}{\partial x^2} - I_4\frac{\partial^2 \ddot{w}_s}{\partial x^2},$$

$$\delta w_s : X\frac{\partial^3 u}{\partial x^3} - F\frac{\partial^4 w_b}{\partial x^4} - H\frac{\partial^4 w_s}{\partial x^4} + S\frac{\partial^2 w_s}{\partial x^2} - k_w\left( w_b + w_s \right) + k_s\left( \frac{\partial^2 w_b}{\partial x^2} + \frac{\partial^2 w_s}{\partial x^2} \right)$$
$$= I_0\left( \ddot{w}_b + \ddot{w}_s \right) - I_2\frac{\partial \ddot{u}}{\partial x} - I_4\frac{\partial^2 \ddot{w}_b}{\partial x^2} - I_5\frac{\partial^2 \ddot{w}_s}{\partial x^2}. \tag{21}$$

## 2.3. NAVIER'S SOLUTION

The present research examines a simply-supported FGS beams. To solve the equations of motion, Navier's solution technique is utilized. The displacement functions of the beam are assumed as the following formulas, where the unknowns are determined through the application of Navier's solution technique.

$$u(x,t) = \sum_{m=1}^{\infty} U_m e^{i\omega t} \cos\alpha_m x$$

$$w_b(x,t) = \sum_{m=1}^{\infty} Wb_m e^{i\omega t} \sin\alpha_m x \tag{22}$$

$$w_s(x,t) = \sum_{m=1}^{\infty} Ws_m e^{i\omega t} \sin\alpha_m x$$

where $\alpha_m = m\pi/L$, $i^2 = -1$, $\omega$ is the natural frequency of the beams, $U_m, Wb_m, Ws_m$ are the unknown coefficients.

Substituting Eq. (22) into Eq. (21), one gets

$$\left( \begin{bmatrix} k_{11} & k_{12} & k_{13} \\ & k_{22} & k_{23} \\ sys & & k_{33} \end{bmatrix} - \omega^2 \begin{bmatrix} m_{11} & m_{12} & m_{13} \\ & m_{22} & m_{23} \\ sys & & m_{33} \end{bmatrix} \right) \begin{Bmatrix} U_m \\ Wb_m \\ Ws_m \end{Bmatrix} = \begin{Bmatrix} 0 \\ 0 \\ 0 \end{Bmatrix} \tag{23}$$

where

$$k_{11} = \alpha^2 A; k_{12} = -\alpha^3 B; k_{13} = -X\alpha^3;$$
$$k_{22} = \alpha^4 D + k_w + k_s\alpha^2; k_{23} = \alpha^4 F + k_w + k_s\alpha^2;$$
$$k_{33} = \alpha^2\left( H\alpha^2 + S \right) + k_w + k_s\alpha^2;$$
$$m_{11} = I_0; m_{12} = I_1\alpha; m_{13} = I_2\alpha;$$
$$m_{22} = I_3\alpha^2 + I_0; m_{23} = I_4\alpha^2 + I_0; m_{33} = I_5\alpha^2 + I_0. \tag{24}$$

The numerical results of the free vibration behavior of the FGS beams are obtained by solving the Eq. (23) using the common manner.

## 3. NUMERICAL RESULTS AND DISCUSSIONS

### 3.1. VERIFICATION STUDY

The FGS beams consist of a homogeneous ceramic core of $Al_2O_3$ and two face-sheets made of FGM of $Al_2O_3/Al$ with varying material properties. Specifically, the metal properties of Aluminum $(Al)$ are characterized by

$$E_m = 70\,\text{GPa}, \nu_m = 0.3, \rho_m = 2702\,\text{kg/m}^3$$

whereas those of ceramic Alumina $(Al_2O_3)$ are described by $E_c = 380\,\text{GPa}, v_c = 0.3, \rho_c = 3960\,\text{kg/m}^3$.

Table 1 presents a comparison of the dimensionless fundamental frequencies obtained from our numerical results with those of Nguyen et a1. [23] and Luat et a1. [18]. Based on the comparison, we can conclude that our numerical results are in agreement with the published data, thus demonstrating the accuracy of our theoretical formulations and calculation program. The dimensionless parameters in table 1 are calculated using the following formulas

$$\bar{\omega} = \omega \frac{L^2}{h} \sqrt{\frac{\rho_m}{E_m}} \qquad\qquad (25)$$

**Table 1:** *The comparison of the natural frequency $\bar{\omega}$ of the FGS beams*

| L/h | k | Sources | Schemes | | | | | |
|-----|---|---------|---------|---------|---------|---------|---------|---------|
| | | | 1-0-1 | 2-1-2 | 2-1-1 | 1-1-1 | 2-2-1 | 1-2-1 |
| 5 | 0 | Nguyen et a1. [23] | 5.1528 | 5.1528 | 5.1528 | 5.1528 | 5.1528 | 5.1528 |
| | | Luat et a1. [18] | 5.1556 | 5.1556 | 5.1556 | 5.1556 | 5.1556 | 5.1556 |
| | | Present | 5.1531 | 5.1531 | 5.1531 | 5.1531 | 5.1531 | 5.1531 |
| | 1 | Nguyen et a1. [23] | 3.5735 | 3.7298 | 3.8206 | 3.8756 | 3.9911 | 4.1105 |
| | | Luat et a1. [18] | 3.5762 | 3.7320 | 3.8221 | 3.8770 | 3.9922 | 4.1108 |
| | | Present | 3.5742 | 3.7303 | 3.8209 | 3.8758 | 3.9913 | 4.1104 |
| | 5 | Nguyen et a1. [23] | 2.7448 | 2.8440 | 2.9789 | 3.0181 | 3.1965 | 3.3771 |
| | | Luat et a1. [18] | 2.7495 | 2.8473 | 2.9811 | 3.0204 | 3.1982 | 3.3775 |
| | | Present | 2.7462 | 2.8451 | 2.9796 | 3.0188 | 3.1970 | 3.3771 |
| | 10 | Nguyen et a1. [23] | 2.6934 | 2.7356 | 2.8715 | 2.8809 | 3.0629 | 3.2357 |
| | | Luat et a1. [18] | 2.6990 | 2.7396 | 2.8740 | 2.8836 | 3.0649 | 3.2365 |
| | | Present | 2.6951 | 2.7369 | 2.8723 | 2.8817 | 3.0635 | 3.2358 |
| 20 | 0 | Nguyen et a1. [23] | 5.4603 | 5.4603 | 5.4603 | 5.4603 | 5.4603 | 5.4603 |
| | | Luat et a1. [18] | 5.4605 | 5.4605 | 5.4605 | 5.4605 | 5.4605 | 5.4605 |
| | | Present | 5.4604 | 5.4604 | 5.4604 | 5.4604 | 5.4604 | 5.4604 |
| | 1 | Nguyen et a1. [23] | 3.7147 | 3.8768 | 3.9775 | 4.0328 | 4.1603 | 4.2889 |
| | | Luat et a1. [18] | 3.7149 | 3.8769 | 3.9776 | 4.0329 | 4.1603 | 4.2889 |
| | | Present | 3.7147 | 3.8768 | 3.9776 | 4.0328 | 4.1603 | 4.2889 |
| | 5 | Nguyen et a1. [23] | 2.8440 | 2.9311 | 3.0776 | 3.1111 | 3.3030 | 3.4921 |
| | | Luat et a1. [18] | 2.8443 | 2.9313 | 3.0777 | 3.1112 | 3.3031 | 3.4922 |
| | | Present | 2.8441 | 2.9311 | 3.0776 | 3.1111 | 3.3031 | 3.4921 |
| | 10 | Nguyen et a1. [23] | 2.8042 | 2.8188 | 2.9665 | 2.9662 | 3.1616 | 3.3406 |
| | | Luat et a1. [18] | 2.8046 | 2.8191 | 2.9666 | 2.9664 | 3.1617 | 3.3407 |
| | | Present | 2.8043 | 2.8189 | 2.9665 | 2.9662 | 3.1616 | 3.3406 |

### 3.2. PARAMETER STUDY

This section investigates the FGS beams composed of (Ti-6Al-4V/Si$_3$N$_4$/Ti-6Al-4V). Specifically, the metal properties of Ti-6Al-4V are characterized by $E_m = 66.2$ GPa, $v_m = 0.3$, $\rho_m = 4420$ kg/m$^3$ and those of ceramic Si$_3$N$_4$ by $E_c = 323$ GPa, $v_c = 0.3$, $\rho_c = 3170$ kg/m$^3$. The beam has a length of $L = 10$ m, and a depth of $b = 1$ m, and is simply supported at both ends. The elastic foundation parameters are dimensionless and defined as $K_w = 20$, $K_s = 5$. For convenience, the following dimensionless quantities are utilized

$$\omega^* = \omega \frac{L^2}{h_0} \sqrt{\frac{\rho_0}{E_0}}; K_w = k_w \frac{L^4}{D_0}; K_w = k_w \frac{L^2}{D_0};$$

$$D_0 = \frac{E_0 h_0^3}{12(1-v^2)}; E_0 = 100 \text{ GPa}; \rho_0 = 1000 \text{ kg/m}^3; h_0 = L/10.$$

(26)

Table 2 shows the dimensionless fundamental frequencies of the FGS beams, while Table 3 presents the dimensionless first six frequencies. As a general observation, increasing the power law index results in a decrease in the frequencies of the FGS beams. This is due to the reduction in the ceramic components, which lowers the stiffness of the beams, consequently reducing their frequencies. For $k = 0$, the frequencies of the FGS beams are independent of their schemes. Moreover, the fundamental frequencies are the smallest, and the frequencies increase with the order of vibration modes.
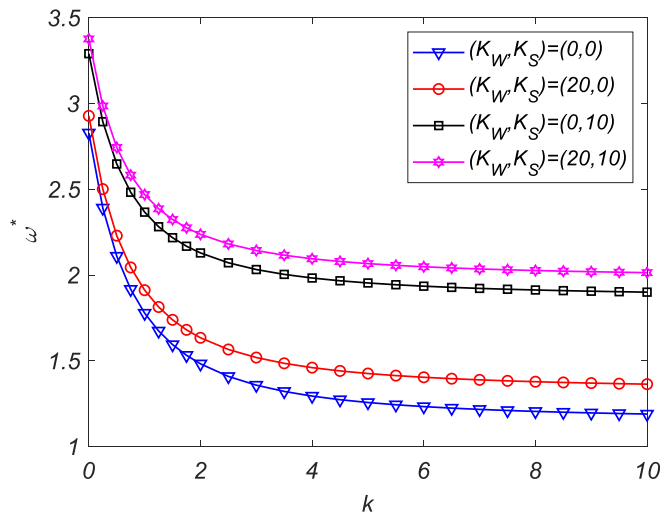
**Table 2:** *The dimensionless fundamental frequency of the FGS beams*

| L/h | k | Schemes | | | | | |
|-----|-----|--------|--------|--------|--------|--------|--------|
|     |     | 1-0-1  | 2-1-2  | 2-1-1  | 2-2-1  | 1-2-1  | 1-8-1  |
| **5** | 0 | 5.4949 | 5.4949 | 5.4949 | 5.4949 | 5.4949 | 5.4949 |
|     | 0.5 | 3.9869 | 4.1735 | 4.2518 | 4.4259 | 4.5452 | 5.0594 |
|     | 1 | 3.3193 | 3.5602 | 3.6678 | 3.9095 | 4.0819 | 4.8424 |
|     | 2 | 2.7648 | 3.0154 | 3.1439 | 3.4274 | 3.6404 | 4.6284 |
|     | 5 | 2.4009 | 2.6001 | 2.7379 | 3.0180 | 3.2448 | 4.4211 |
|     | 10 | 2.3110 | 2.4750 | 2.6120 | 2.8715 | 3.0905 | 4.3306 |
| **10** | 0 | 3.1606 | 3.1606 | 3.1606 | 3.1606 | 3.1606 | 3.1606 |
|     | 0.5 | 2.4089 | 2.5002 | 2.5388 | 2.6247 | 2.6838 | 2.9410 |
|     | 1 | 2.0938 | 2.2083 | 2.2596 | 2.3756 | 2.4589 | 2.8330 |
|     | 2 | 1.8431 | 1.9592 | 2.0180 | 2.1501 | 2.2503 | 2.7275 |
|     | 5 | 1.6826 | 1.7756 | 1.8364 | 1.9643 | 2.0685 | 2.6261 |
|     | 10 | 1.6426 | 1.7201 | 1.7801 | 1.8987 | 1.9988 | 2.5821 |
| **20** | 0 | 2.4595 | 2.4595 | 2.4595 | 2.4595 | 2.4595 | 2.4595 |
|     | 0.5 | 2.1367 | 2.1802 | 2.1960 | 2.2347 | 2.2615 | 2.3692 |
|     | 1 | 2.0081 | 2.0633 | 2.0838 | 2.1354 | 2.1724 | 2.3258 |
|     | 2 | 1.9050 | 1.9650 | 1.9881 | 2.0475 | 2.0916 | 2.2839 |
|     | 5 | 1.8299 | 1.8884 | 1.9128 | 1.9742 | 2.0216 | 2.2440 |
|     | 10 | 1.8049 | 1.8616 | 1.8861 | 1.9468 | 1.9941 | 2.2268 |

**Table 3:** *The dimensionless first six frequencies of the FGS beams*

| Scheme | $k$ | Mode 1 | Mode 2 | Mode 3 | Mode 4 | Mode 5 | Mode 6 |
|--------|-----|--------|--------|--------|--------|--------|--------|
| **1-0-1** | 0 | 3.1606 | 11.0901 | 23.0613 | 37.8154 | 54.3954 | 72.1506 |
| | 0.5 | 2.4089 | 8.0952 | 16.8635 | 27.8835 | 40.4798 | 54.1568 |
| | 1 | 2.0938 | 6.7757 | 14.0703 | 23.3275 | 34.0017 | 45.6773 |
| | 2 | 1.8431 | 5.6850 | 11.7177 | 19.4343 | 28.3987 | 38.2691 |
| | 5 | 1.6826 | 4.9716 | 10.1342 | 16.7397 | 24.4181 | 32.8808 |
| | 10 | 1.6426 | 4.7946 | 9.7066 | 15.9436 | 23.1424 | 31.0284 |
| **2-2-1** | 0 | 3.1606 | 11.0901 | 23.0613 | 37.8154 | 54.3954 | 72.1506 |
| | 0.5 | 2.6247 | 8.9664 | 18.6982 | 30.8754 | 44.7394 | 59.7418 |
| | 1 | 2.3756 | 7.9439 | 16.5614 | 27.4297 | 39.8901 | 53.4510 |
| | 2 | 2.1501 | 6.9919 | 14.5468 | 24.1499 | 35.2380 | 47.3781 |
| | 5 | 1.9643 | 6.1861 | 12.8187 | 21.3080 | 31.1740 | 42.0384 |
| | 10 | 1.8987 | 5.8982 | 12.1947 | 20.2722 | 29.6808 | 40.0628 |
| **1-8-1** | 0 | 3.1606 | 11.0901 | 23.0613 | 37.8154 | 54.3954 | 72.1506 |
| | 0.5 | 2.9410 | 10.2247 | 21.2909 | 35.0073 | 50.4921 | 67.1302 |
| | 1 | 2.8330 | 9.7939 | 20.4044 | 33.5944 | 48.5204 | 64.5859 |
| | 2 | 2.7275 | 9.3694 | 19.5276 | 32.1931 | 46.5612 | 62.0548 |
| | 5 | 2.6261 | 8.9583 | 18.6759 | 30.8295 | 44.6530 | 59.5893 |
| | 10 | 2.5821 | 8.7790 | 18.3036 | 30.2332 | 43.8185 | 58.5120 |

This paragraph investigates the impact of the power-law index on the dimensionless fundamental frequency of FGS beams having $L/h = 10$. The results, presented in figure 2, demonstrate that the frequencies of the FGS beams decrease as the material index $k$ increases. Furthermore, the elastic foundations significantly affect the vibration behavior of the FGS beams.
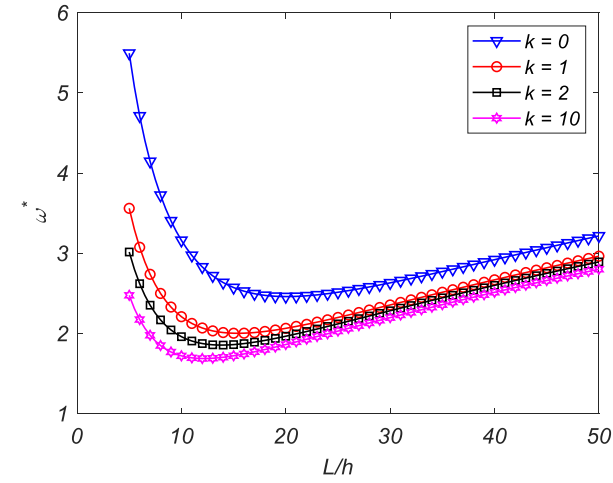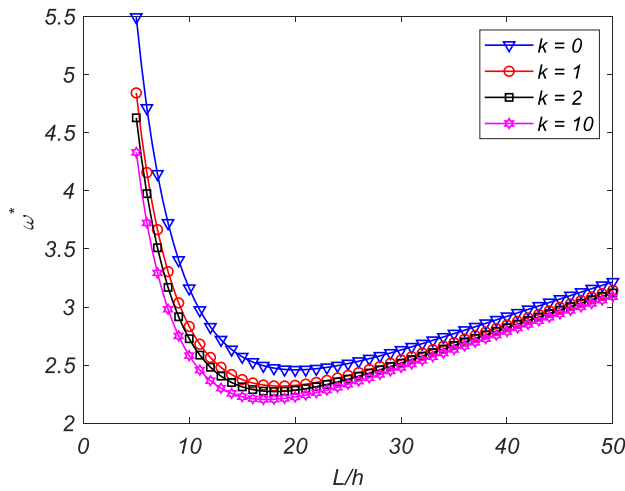


a) (2-1-2)
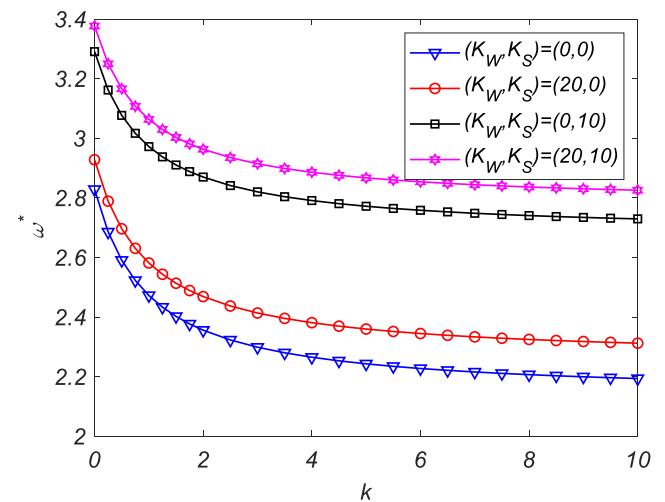


b) (1-8-1)

**Fig. 2.** The variation of the dimensionless fundamental frequencies of the FGS beams with $L/h = 10$

Figure 3; illustrates the impact of the length-to-height ratio on the dimensionless fundamental frequency of FGS beams with $K_w = 20$, $K_s = 5$. As observed from the figure, the frequencies of the FGS beams decrease rapidly and then increase as the length-to-height ratio $L/h$ increases, reaching the minimum values. This

phenomenon is discovered for the first time in this study and should be considered when designing and manufacturing FGS beam structures to prevent resonance.



a) (2-1-2)



b) (1-8-1)

**Fig. 3.** The variation of the dimensionless fundamental frequencies of the FGS beams with $K_w = 20, K_s = 5$



a) $K_S = 5$



b) $K_W = 20$

**Fig. 4.** The variation of the dimensionless fundamental frequencies of the (2-1-2) FGS beams with $L / h = 10$

Figure 4; demonstrates the impact of the elastic foundation parameters on the dimensionless fundamental frequency of (2-1-2) FGS beams with $L / h = 10$. The figure reveals that the elastic foundations have a significant influence on the free vibration of the FGS beams. As the parameters of the Pasternak's foundations increase, the frequencies of the FGS beam quickly rise. Furthermore, it is apparent that the parameter $k_s$ has a more pronounced effect than parameter $k_w$ on the elastic foundations.
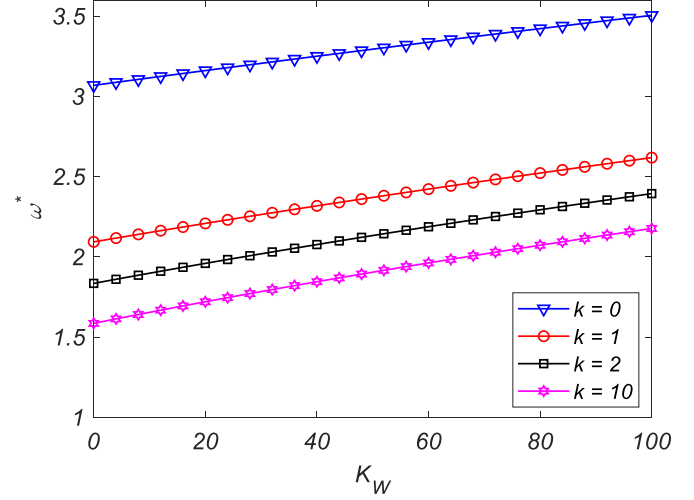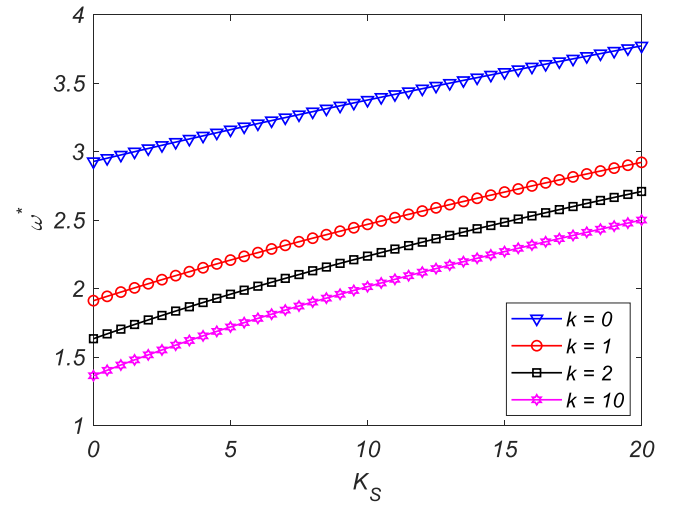
## 4. CONCLUSIONS

This study introduced a refined higher-order shear deformation theory for the free vibration analysis of FGS beams, which considers the parabolic distribution of the transverse shear strain and stress through the thickness of the beams. The proposed theory eliminates the shear locking phenomenon without using a shear correction factor. The comparison study confirms the accuracy and efficiency of the proposed theoretical and calculation program. Additionally, the study investigates the effects of some parameters on the vibration behaviors of the FGS beams. Notably, the study reveals that as the length-to-height ratio increases, there is a minimum value of frequency of the FGS beams. These findings can serve as

benchmarks for future works on the free vibration analysis of FGS beams, which have significant potential applications in engineering and industry.

## 5. REFERENCES

[1] J.N. Reddy, Analysis of functionally graded plates, Int. J. Numer. Methods Eng. 47 (2000) 663–684. https://doi.org/https://doi.org/10.1002/(SICI)1097-0207(20000110/30)47:1/3<663::AID-NME787>3.0.CO;2-8.

[2] A. Chakraborty, S. Gopalakrishnan, J.N. Reddy, A new beam finite element for the analysis of functionally graded materials, Int. J. Mech. Sci. 45 (2003) 519–539. https://doi.org/10.1016/S0020-7403(03)00058-4.

[3] P.R. Heyliger, J.N. Reddy, A higher order beam finite element for bending and vibration problems, J. Sound Vib. 126 (1988) 309–326. https://doi.org/https://doi.org/10.1016/0022-460X(88)90244-1.

[4] P. Van Vinh, N. Van Chinh, A. Tounsi, Static bending and buckling analysis of bi-directional functionally graded porous plates using an improved first-order shear deformation theory and FEM, Eur. J. Mech. A/Solids. 96 (2022) 104743. https://doi.org/10.1016/j.euromechsol.2022.104743.

[5] P. Van Vinh, A. Tounsi, Free vibration analysis of functionally graded doubly curved nanoshells using nonlocal first-order shear deformation theory with variable nonlocal parameters, Thin-Walled Struct. 174 (2022) 109084. https://doi.org/10.1016/j.tws.2022.109084.

[6] S.S. Akavci, A.H. Tanrikulu, 8. Static and free vibration analysis of functionally graded plates based on a new quasi-3D and 2D shear deformation theories, Compos. Part B Eng. 83 (2015) 203–215. https://doi.org/https://doi.org/10.1016/j.compositesb.2015.08.043.

[7] K. Bouafia, A. Kaci, M.S.A. Houari, A. Benzair, A. Tounsi, A nonlocal quasi-3D theory for bending and free flexural vibration behaviors of functionally graded nanobeams, Smart Struct. Syst. 19 (2017) 115–126. https://doi.org/10.12989/sss.2017.19.2.115.

[8] Z. hai Wang, X. hong Wang, G. dong Xu, S. Cheng, T. Zeng, Free vibration of two-directional functionally graded beams, Compos. Struct. 135 (2016) 191–198. https://doi.org/10.1016/j.compstruct.2015.09.013.

[9] D.K. Nguyen, Large displacement behaviour of tapered cantilever Euler-Bernoulli beams made of functionally graded material, Appl. Math. Comput. 237 (2014) 340–355.

https://doi.org/10.1016/j.amc.2014.03.104.

[10] J.W. Lee, J.Y. Lee, Free vibration analysis of functionally graded Bernoulli-Euler beams using an exact transfer matrix expression, Int. J. Mech. Sci. 122 (2017) 1–17. https://doi.org/https://doi.org/10.1016/j.ijmecsci.2017.01.011.

[11] A. Shahba, S. Rajasekaran, Free vibration and stability of tapered Euler-Bernoulli beams made of axially functionally graded materials, Appl. Math. Model. 36 (2012) 3094–3111. https://doi.org/10.1016/j.apm.2011.09.073.

[12] P. Van Vinh, L.T. Son, A new first-order mixed beam element for static bending analysis of functionally graded graphene oxide powder-reinforced composite beams, Structures. 36 (2022) 463–472. https://doi.org/10.1016/j.istruc.2021.12.032.

[13] P. Van Vinh, N.Q. Duoc, N.D. Phuong, A New Enhanced First-Order Beam Element Based on Neutral Surface Position for Bending Analysis of Functionally Graded Porous Beams, Iran. J. Sci. Technol. - Trans. Mech. Eng. (2022) 1–16. https://doi.org/10.1007/s40997-022-00485-1.

[14] T.K. Nguyen, T.P. Vo, H.T. Thai, Static and free vibration of axially loaded functionally graded beams based on the first-order shear deformation theory, Compos. Part B Eng. 55 (2013) 147–157. https://doi.org/10.1016/j.compositesb.2013.06.011.

[15] Z. Zhang, Y. Li, H. Wu, H. Zhang, H. Wu, S. Jiang, G. Chai, Mechanical analysis of functionally graded graphene oxide-reinforced composite beams based on the first-order shear deformation theory, Mech. Adv. Mater. Struct. 27 (2020) 3–11. https://doi.org/10.1080/15376494.2018.1444216.

[16]    P. Van Vinh, Static bending analysis of functionally graded sandwich beams using a novel mixed beam element based on first-order shear deformation theory, Forces Mech. 4 (2021) 100039. https://doi.org/10.1016/j.finmec.2021.100039.

[17]    T.-K. Nguyen, T. Truong-Phong Nguyen, T.P. Vo, H.-T. Thai, Vibration and buckling analysis of functionally graded sandwich beams by a new higher-order shear deformation theory, Compos. Part B Eng. 76 (2015) 273–285. https://doi.org/https://doi.org/10.1016/j.compositesb.2015.02.032.

[18]    D.T. Luat, D. Van Thom, T.T. Thanh, P. Van Minh, T. Van Ke, P. Van Vinh, Mechanical analysis of bi-functionally graded sandwich nanobeams, Adv. Nano Res. 11 (2021) 55–71. https://doi.org/10.12989/anr.2021.11.1.055.

[19]    H.-T. Thai, T.P. Vo, Bending and free vibration of functionally graded beams using various higher-order shear deformation beam theories, Int. J. Mech. Sci. 62 (2012) 57–66. https://doi.org/https://doi.org/10.1016/j.ijmecsci.2012.05.014.

[20]    M.A. Uddin, A.H. Sheikh, T. Bennett, B. Uy, Large deformation analysis of two layered composite beams with partial shear interaction using a higher order beam theory, Int. J. Mech. Sci. 122 (2017) 331–340. https://doi.org/10.1016/j.ijmecsci.2017.01.030.

[21]    G. He, D. Wang, X. Yang, Analytical Solutions for Free Vibration and Buckling of Composite Beams Using a Higher Order Beam Theory, Acta Mech. Solida Sin. 29 (2016) 300–315. https://doi.org/10.1016/S0894-9166(16)30163-X.

[22]    G. He, X. Yang, Dynamic analysis of two-layer composite beams with partial interaction using a higher order beam theory, Int. J. Mech. Sci. 90 (2015) 102–112. https://doi.org/10.1016/j.ijmecsci.2014.10.020.

[23]    T.-K. Nguyen, B.-D. Nguyen, A new higher-order shear deformation theory for static, buckling and free vibration analysis of functionally graded sandwich beams, J. Sandw. Struct. Mater. 17 (2015) 613–631. https://doi.org/10.1177/1099636215589237.

[24]    M. Askari, E. Brusa, C. Delprete, On the vibration analysis of coupled transverse and shear piezoelectric functionally graded porous beams with higher-order theories, J. Strain Anal. Eng. Des. 56 (2020) 29–49. https://doi.org/10.1177/0309324720922085.

[25]    B. Riadh, A.H. Ait, T. Abdelouahed, A new higher-order shear and normal deformation theory for functionally graded sandwich beams, Steel Compos. Struct. 19 (2015) 521–546. https://doi.org/10.12989/SCS.2015.19.3.521.

[26]    W. Li, H. Ma, W. Gao, A higher-order shear deformable mixed beam element model for accurate analysis of functionally graded sandwich beams, Compos. Struct. 221 (2019) 110830. https://doi.org/https://doi.org/10.1016/j.compstruct.2019.04.002.

[27]    A. Frikha, A. Hajlaoui, M. Wali, F. Dammak, A new higher order C0 mixed beam element for FGM beams analysis, Compos. Part B Eng. 106 (2016) 181–189. https://doi.org/https://doi.org/10.1016/j.compositesb.2016.09.024.

[28]    X.-F. Li, B.-L. Wang, J.-C. Han, A higher-order theory for static and dynamic analyses of functionally graded beams, Arch. Appl. Mech. 80 (2010) 1197–1212. https://doi.org/10.1007/s00419-010-0435-6.

[29]    M. Şimşek, Fundamental frequency analysis of functionally graded beams by using different higher-order beam theories, Nucl. Eng. Des. 240 (2010) 697–705. https://doi.org/10.1016/j.nucengdes.2009.12.013.

[30]    A. Karamanli, T.P. Vo, A quasi-3D theory for functionally graded porous microbeams based on the modified strain gradient theory, Compos. Struct. 257 (2021) 113066. https://doi.org/https://doi.org/10.1016/j.compstruct.2020.113066.

[31]    A.I. Osofero, T.P. Vo, T.-K. Nguyen, J. Lee, Analytical solution for vibration and buckling of functionally graded sandwich beams using various quasi-3D theories, J. Sandw. Struct. Mater. 18 (2015) 3–29. https://doi.org/10.1177/1099636215582217.

[32]    T.P. Vo, H.-T. Thai, T.-K. Nguyen, F. Inam, J.

Lee, A quasi-3D theory for vibration and buckling of functionally graded sandwich beams, Compos. Struct. 119 (2015) 1–12. https://doi.org/https://doi.org/10.1016/j.compstruct.2014.08.006.

[33]    T. Yu, J. Zhang, H. Hu, T.Q. Bui, A novel size-dependent quasi-3D isogeometric beam model for two-directional FG microbeams analysis, Compos. Struct. 211 (2019) 76–88. https://doi.org/https://doi.org/10.1016/j.compstruct.2018.12.014.

[34]    W. Fang, T. Yu, L. Van Lich, T.Q. Bui, Analysis of thick porous beams by a quasi-3D theory and isogeometric analysis, Compos. Struct. 221 (2019) 110890. https://doi.org/https://doi.org/10.1016/j.compstruct.2019.04.062.